

# POINT-MoE: LARGE-SCALE MULTI-DATASET TRAINING WITH MIXTURE-OF-EXPERTS FOR 3D SEMANTIC SEGMENTATION

Xuweiyi Chen<sup>1</sup>   Wentao Zhou<sup>1</sup>   Aruni RoyChowdhury<sup>2</sup>   Zezhou Cheng<sup>1</sup>

<sup>1</sup>University of Virginia   <sup>2</sup>MathWorks

<https://point-moe.cs.virginia.edu/>

## ABSTRACT

While massively scaling both data and models have become central in NLP and 2D vision, their benefits for 3D point cloud understanding remain limited. We study the initial step of scaling 3D point cloud understanding under a realistic regime: large-scale multi-dataset joint training for 3D semantic segmentation, with no dataset labels available at training or inference time. Point clouds arise from a wide range of sensors (*e.g.*, depth cameras, LiDAR) and scenes (*e.g.*, indoor, outdoor), yielding heterogeneous scanning patterns, sampling densities, and semantic biases; naively mixing such datasets degrades standard models. Therefore, we introduce **Point-MoE**, a Mixture-of-Experts design that expands model capacity through sparsely activated expert MLPs and a lightweight top- $k$  router, allowing tokens to select specialized experts without requiring dataset supervision. Trained jointly on a diverse mix of indoor and outdoor datasets, and evaluated on seen datasets as well as in zero-shot settings, Point-MoE outperforms prior methods without using dataset labels for either training or inference. This outlines a scalable path for 3D perception: letting the model discover structure in heterogeneous 3D data rather than imposing it via manual curation or dataset-specific heuristics.

## 1 INTRODUCTION

In both language and vision, we have witnessed remarkable advances driven by two trends: the aggregation of massive, heterogeneous datasets [4, 8, 58, 61, 66, 97], and the deployment of ever-larger models trained on them in a unified manner [7, 16, 21, 36, 51, 57]. These models succeed not because they are crafted for a specific dataset, but because they learn underlying regularities across multiple datasets. However, 3D point cloud understanding has not yet followed the same trajectory, despite its wide applications in robotics [11, 53, 90], autonomous systems [12, 13, 43], augmented reality [6, 77], and embodied intelligence [72, 79]. Taking 3D semantic segmentation as an example, although diverse 3D datasets exist—such as ScanNet [19], SemanticKITTI [5], nuScenes [9], and ASE [2]—each covers only a narrow slice of real-world variation. Point clouds arise from diverse pipelines (RGB-D, LiDAR, multi-view stereo), each with their own distinct densities, artifacts, and semantic biases (Fig. 1, left). The result is a rich yet siloed ecosystem of 3D models, where models trained on one domain often fail to generalize to others.

A natural response is to *train across silos*, presumably resulting in a single set of model parameters that is effective across the spectrum of datasets. One might, for example, naively train the state-of-the-art Point Transformer V3 (PTv3) [81] (Fig. 1a) on a mixture of datasets from multiple domains, *e.g.* indoor and outdoor. In practice, however, such models struggle to reconcile the heterogeneity of the data distribution even as capacity scales (Tab. 1). To mitigate this, recent methods have introduced dataset-aware components. Point Prompt Training (PPT) [82] (Fig. 1b) assigns dataset-specific normalization layers, while One-for-All [75] uses a lightweight dataset classifier with dataset-specific adapters. While effective, these methods rely on dataset labels, identifying which specific dataset an input sample originated from, during training and inference. Moreover, adapting only the normalization parameters may be insufficient for large-scale multi-dataset training.

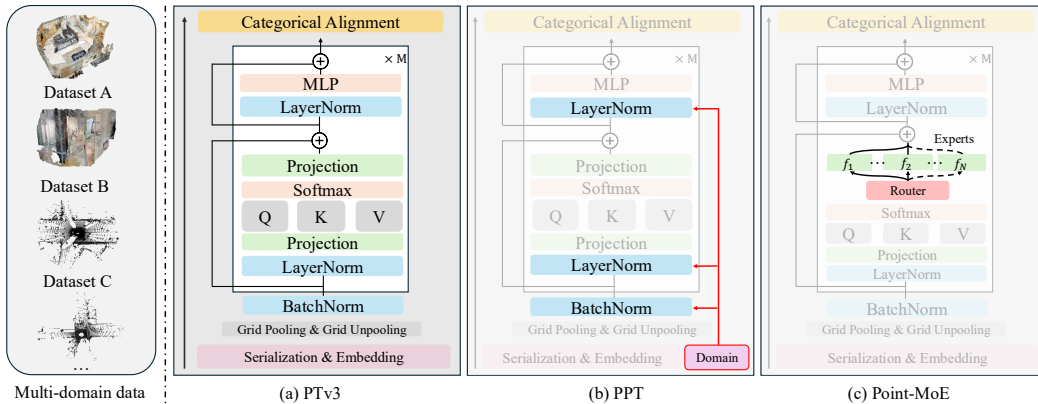


Figure 1: **Overview of multi-datasets training architectures.** Point clouds exhibit diverse characteristics across datasets. (a) Naively training Point Transformer V3 (PTv3) [81] on multi-datasets data leads to degraded performance within each domain. (b) Point Prompt Training (PPT) [82] addresses this by adding dataset-aware normalization parameters. (c) Our proposed Point-MoE tackles this challenge with Mixture-of-Experts (MoE), enabling dynamic expert specialization across datasets.

At deployment, point clouds arrive from mixed, unlabeled sources with unknown provenance, *i.e.* there is no oracle “dataset ID” available during inference. Accordingly, we study a realistic regime: **large-scale multi-dataset joint training** for 3D semantic segmentation with **no dataset labels at inference**. We hypothesize that Mixture-of-Experts (MoE) architectures [30, 34] are well-suited to this setting. We introduce **Point-MoE**, a sparse MoE model built upon PTv3 [81]. As illustrated in Fig. 1c, Point-MoE replaces each attention projection layer in each PTv3 block with a MoE module composed of expert MLPs and a lightweight router that selects a sparse top- $k$  subset of experts per token. Our design is motivated by three insights. First, MoE encourages expert specialization and token-to-expert routing [15, 87], enabling a single model to learn from mixed datasets without access to dataset labels at training or test time. Second, compared to normalization-based adaptations such as PPT [82] and One-for-All [75], MoE offers far more expressive capacity to model dataset-specific variations. Third, sparse MoE architectures maintain computational efficiency during training and inference, and are a standard mechanism for scaling large models in NLP and 2D vision [20, 22, 24, 40, 59]. We extend these benefits, well-established in language and 2D vision, to 3D point cloud understanding, focusing on 3D semantic segmentation. We conduct extensive experiments across a diverse collection of 3D datasets spanning indoor and outdoor scenes, synthetic and real datasets, and multiple sensor modalities. We evaluate on both in-domain and zero-shot datasets, all without dataset labels. To comprehensively assess Point-MoE, we evaluate both in-domain (seen) datasets and out-of-domain (zero-shot) datasets, all without access to dataset labels. Our goal is to demonstrate that Point-MoE not only achieves strong performance on seen datasets but also generalizes robustly to unseen distributions, without relying on dataset-specific augmentation or supervision. Across both regimes, Point-MoE consistently outperforms competitive multi-dataset baselines. We further ablate the number of experts, sparsity level, and MoE placement (Tab. 3), and find that Point-MoE learns coherent routing patterns and exhibits organic expert specialization driven by the underlying data distribution (Fig. 2, 3, 4).

To the best of our knowledge, this work provides the first systematic study of MoE for 3D point cloud understanding under the large-scale multi-dataset training regime. Our contributions are: (1) we focus on multi-dataset 3D semantic segmentation without domain labels, using a single model, and put forth Mixture-of-Experts as a natural solution to this task; (2) we carefully explore the MoE design space and provide extensive ablations that highlight the trade-offs and inform effective configurations; (3) we demonstrate that Point-MoE achieves state-of-the-art performance across seven datasets under this protocol while maintaining inference efficiency; and (4) we analyze token-level routing trajectories and expert usage, revealing encoder-decoder specialization patterns consistent with 3D geometry. Together, these findings point toward a scalable path for 3D perception: rather than building separate models for each dataset or domain, a single unified system can adapt across the spectrum of 3D data sources, leveraging scaling laws for data and compute [68].

## 2 RELATED WORK

**Point Cloud understanding.** Deep learning backbones for 3D scene understanding can be broadly categorized by how they process point clouds: projection-based methods [13, 38, 41, 64], voxel-based methods [17, 25, 49, 63], and point-based methods [54, 55, 69, 93]. More recently, transformer-based architectures operating on point clouds have emerged as strong contenders in this space [27, 80, 81, 94]. Among them, Point Transformer V3 (PTv3) [81] represents the current state of the art, introducing a novel space-filling curve based serialization scheme, that transforms the unstructured 3D points into a 1D sequence, enabling efficient transformer-based modeling. Recent works [32, 39, 82, 83, 96] scale point cloud understanding models to multi-dataset settings and show that large-scale point cloud data can improve performance on specific datasets: Sonata [83] explores multi-dataset self-supervised learning, but does not train across indoor and outdoor datasets. On the other hand, Point Prompt Training (PPT) [82] demonstrates that using dataset-specific normalization layers during pretraining improves 3D semantic segmentation performance across multiple datasets along with dataset-specific fine-tuning. In 3D detection, One-for-All [75] adopts a sparse convolutional network with dataset-specific partitions and normalization layers to boost multi-datasets performance, and UniDet3D [37] achieves state-of-the-art performance with multi-dataset joint training by merging label spaces across datasets into unified taxonomy and building upon vanilla transformer [71] architecture. Rather than relying on dataset-specific preprocess or architectural branches [75, 82], we propose a unified sparse expert framework that learns to specialize dynamically across various datasets, without requiring explicit dataset labels during training or inference.

**Mixture-of-Experts.** Mixture-of-Experts (MoE) [30, 34] increases model capacity without proportional compute by activating only a subset of experts per input [62]. This conditional computation has powered trillion-scale NLP models [20, 22, 24, 33, 40, 46, 47, 98] and demonstrated similar efficiency in vision [59]. Beyond scaling, MoE is naturally suited for heterogeneous or multi-datasets data, as experts tend to self-organize by dataset or task. Prior work has shown improvements in multi-source sentiment analysis and POS tagging [26], dataset-adaptive language modeling [28], automatic chart understanding [87], and multilingual translation [15]. Mod-Squad [14] introduced modular expert routing for multi-task learning, balancing cooperation and specialization. Similar trends are observed in vision and vision-language applications: DAMEX [31], MoE-LLaVA [44] and DeepSeek-VL [48, 85]. To our knowledge, this is the first work to extend MoE to multi-dataset training in 3D point clouds. MoE3D [76] recently introduces a MoE formulation for 3D reconstruction.

**Domain generalization.** Classical domain generalization (DG) trains on one or more labeled source domains and targets zero-shot performance on a specified target domain, typically in sensor- and semantic-ontology-homogeneous outdoor LiDAR settings [35, 60, 84, 86, 88, 92]. We instead study large-scale joint training on heterogeneous datasets with naturally misaligned label spaces, evaluating a single model on both seen and zero-shot datasets. Unlike DG, our goal is a single unified model for heterogeneous multi-dataset learning rather than transfer to a fixed target domain, although DG methods remain complementary and could be layered onto Point-MoE as a natural extension.

## 3 POINT-MOE FOR MULTI-DATASET POINT CLOUD TRAINING

### 3.1 LARGE-SCALE MULTI-DATASET JOINT TRAINING

**Task definition.** Given a 3D scene represented as a point cloud  $\mathcal{P} = \{p_i\}_{i=1}^M$ , where each point  $p_i \in \mathbb{R}^3$  denotes XYZ coordinates, semantic segmentation aims to predict a single class label  $\hat{y}_i \in \mathcal{C}$  for each point  $p_i$  from a fixed label set  $\mathcal{C} = \{c_1, c_2, \dots, c_m\}$ . Predicted labels for the entire point cloud are compactly denoted as  $\hat{\mathbf{y}}$ . Similarly, we denote the corresponding ground-truth labels by  $\mathbf{y} = [y_1, y_2, \dots, y_M]$ ,  $y_i \in \mathcal{C}$ , where  $y_i$  is the true semantic label of point  $p_i$ .

Let a dataset containing multiple point clouds be denoted as  $\mathcal{D} = \{(\mathcal{P}_t, \mathbf{y}_t)\}_{t=1}^{|\mathcal{D}|}$ . The complete training set across multiple datasets is then  $\mathbb{D} = \{\mathcal{D}_j\}_{j=1}^{|\mathbb{D}|}$ . The goal of our multi-dataset joint training is to learn a unified model (*i.e.* a single set of model parameters, without resorting to per-dataset fine-tuning) over all datasets that minimizes prediction error across  $\mathbb{D}$ , while also generalizing effectively to zero-shot datasets drawn from distributions unseen at training time.

Let  $\Phi_\theta$  denote a segmentation model with parameters  $\theta$ , that takes in a point cloud  $\mathcal{P}$  and predicts per-point class labels  $\hat{\mathbf{y}}$ . Let  $\mathcal{L}(\mathbf{y}, \hat{\mathbf{y}})$  denote the loss, *e.g.* cross-entropy, on a point cloud between ground-truth segmentation labels  $\mathbf{y}$  and predicted labels  $\hat{\mathbf{y}}$ . Formally, the training objective is  $\min_\theta \mathbb{E}_{\mathcal{D}_j \sim \mathbb{D}} \mathbb{E}_{(\mathcal{P}, \mathbf{y}) \sim \mathcal{D}_j} [\mathcal{L}(\mathbf{y}, \Phi_\theta(\mathcal{P}))]$ . We do not assume oracle dataset labels at training or inference. In other words, we do not know which dataset a sample is drawn from.

We can formally contrast this to alternate multi-dataset objective formulations such as [75, 82], that learn an explicit set of dataset-specific parameters  $\omega_j$ , along with  $\theta$ :  $\min_{\theta, \{\omega_j\}} \mathbb{E}_{\mathcal{D}_j \sim \mathbb{D}} \mathbb{E}_{(\mathcal{P}, \mathbf{y}) \sim \mathcal{D}_j} [\mathcal{L}(\mathbf{y}, \Phi_{\theta, \omega_j}(\mathcal{P}))]$ . PPT [82] instantiates  $\{\omega_j\}_{j=1}^{|\mathbb{D}|}$  as the learnable gain and bias terms of the normalization layers of PTv3, trained on a per-dataset basis. During inference, the source dataset  $\mathcal{D}_j$  of an incoming point cloud  $\mathcal{P}$  must be identified in order to apply the correct normalization  $\omega_j$ , usually obtained from a lightweight dataset classifier as in One-for-All [75].

**Language-guided classification.** To bridge label discrepancies across datasets (*i.e.*  $\mathcal{C}_i \neq \mathcal{C}_j$  for datasets  $\mathcal{D}_i$  and  $\mathcal{D}_j$ ), we project per-point features to a shared language space using CLIP [57] text embeddings, following PPT [82]. This enables supervision via class names, without relying on dataset labels. For instance, the class “pillow” is missing in ScanNet (grouped as “other”) but explicitly labeled in Structured3D; aligning to the CLIP embedding of “pillow” transfers knowledge across datasets even without direct supervision. All baselines and our Point-MoE are adapted to this language-guided protocol, ensuring fair comparison.

### 3.2 POINT-MOE

**Mixture-of-Experts (MoE) layer.** Mixture-of-Experts [30] is a conditional computation architecture enabling significant capacity expansion while only modestly increasing computational cost. The core of MoE is to route input tokens dynamically to specialized subnetworks, referred to as experts, via a lightweight gating mechanism. Given an input feature vector  $\mathbf{x} \in \mathbb{R}^D$ , each MoE layer contains  $N$  experts  $\{f_i\}_{i=1}^N$  where  $f_i : \mathbb{R}^D \rightarrow \mathbb{R}^D$  and a gating network  $G : \mathbb{R}^D \rightarrow \mathbb{R}^N$ . For each input  $\mathbf{x}$ , the MoE layer output is computed as a weighted sum over the top- $k$  activated experts:

$$\text{MoE}(\mathbf{x}) = \sum_{i \in \mathcal{S}_x} G_i(\mathbf{x}) f_i(\mathbf{x}), \quad (1)$$

where  $\mathcal{S}_x$  is the top- $k$  expert set and  $G_i(\mathbf{x})$  are normalized gate weights. In practice,  $G$  is a linear projection followed by a sparse softmax, activating only  $k \ll N$  experts. Importantly, MoE introduces a large design space, including the choice of which components to replace, the number of experts, the routing strategy, whether to do auxiliary balancing loss and whether to use top-1 or top-2 gating. We systematically study how different MoE configurations affect performance on 3D point clouds through detailed ablations in the experiments.

**Integration into PTv3.** Given a point cloud  $\mathcal{P}$  with  $M$  points, PTv3 [81] serializes and embeds the input into a token sequence  $\mathbf{Z} = [z_1, \dots, z_M]$ . PTv3 then applies stacked multi-head self-attention (MHSA) blocks interleaved with up- and down-sampling for multi-scale reasoning on these per-token embeddings. At any intermediate layer  $\ell$ , let  $\mathbf{x}_\ell \in \mathbb{R}^{M \times D}$  denote the token sequence at layer  $\ell$ , where  $D$  is the feature dimension,  $H$  is the number of heads in multi-head attention, and FFN denotes a feed-forward network. The computations of a self-attention block using standard QKV-formulation and pre-norm residuals is as follows:

$$\mathbf{X} = \text{Norm}(\mathbf{x}_{\ell-1}), \quad \mathbf{Q} = \mathbf{X}W_q, \mathbf{K} = \mathbf{X}W_k, \mathbf{V} = \mathbf{X}W_v, \quad (2)$$

$$\mathbf{A} = \text{Softmax}(\mathbf{Q}\mathbf{K}^\top / \sqrt{d_h}) \mathbf{V}, \quad d_h = D/H, \quad (3)$$

$$\mathbf{O} = W_o \mathbf{A}, \quad (4)$$

$$\mathbf{x}'_\ell = \mathbf{x}_{\ell-1} + \mathbf{O}, \quad (5)$$

$$\mathbf{x}_\ell = \mathbf{x}'_\ell + \text{FFN}(\text{Norm}(\mathbf{x}'_\ell)) \quad (6)$$

The learnable query, key, and value projections are denoted as  $W_q$ ,  $W_k$  and  $W_v$ , while  $W_o$  denotes the projection applied on the attention output  $\mathbf{A}$ . We apply MoE only at the *attention output projection* ( $W_o$ ) in every block, rewriting Eq. (4) as  $\mathbf{O} = \text{MoE}(\mathbf{A})$ ; the query, key, and value projections ( $W_q$ ,  $W_k$ ,  $W_v$ ) remain dense. Empirically, placing MoE at  $W_o$  yields better performance than placing it in the FFN under the same expansion (Tab. 3d). We hypothesize that the gain comes from adding

nonlinearity and capacity on the projection path: with purely linear projections, the composition of  $W_v$  and  $W_o$  can be merged into a single projection [47].

Beyond MoE-layer placement, we employ *mixed-dataset training*: each minibatch jointly samples from both indoor and outdoor data (Tab. 4). Having tokens from multiple datasets within a single minibatch, and thus contributing to the gradients of one update step, is useful in facilitating cross-sample interaction and emergent expert specialization.

To illustrate the general applicability of this framework, we further extend MoE to OA-CNNs [52], a sparse convolution backbone. MoE-augmented OA-CNNs likewise outperform the dense version, further underscoring the effectiveness and general applicability of MoE as it is not tied to a specific backbone architecture. Detailed results are in the supplementary material under Sec. B.2.

## 4 EXPERIMENTS

We conduct comprehensive experiments to evaluate Point-MoE for 3D semantic segmentation. First, we describe baseline methods and experimental setups (Sec. 4.1). Then, we present detailed empirical results under two primary joint training scenarios: (1) indoor-only, and (2) combined indoor-outdoor training (Sec. 4.2). Finally, we provide ablation studies that highlight key design choices of the MoE architecture (Sec. 4.3) and detailed analysis of MoE behaviors (Sec. 4.4).

### 4.1 EXPERIMENTAL SETUP

**Datasets.** We conduct experiments on three indoor benchmarks: ScanNet [19], S3DIS [1], and Structured3D [95], and additionally evaluate zero-shot on Matterport3D [10]. Specifically, we train a single model on ScanNet, S3DIS, and Structured3D, and directly evaluate its performance on both seen and unseen datasets via the language-guided head using the same checkpoint. We further test the best-performing Point-MoE architectures and baseline configurations in a more challenging indoor and outdoor joint setting that incorporates nuScenes [9] and SemanticKITTI [5] as training data, and Waymo [67] for zero-shot evaluation. The same evaluation protocol is used across both settings.

**Baselines.** Since Point-MoE is built on PTv3 [81], we adopt PTv3 and PPT [82] as our primary baselines. PPT, originally designed with dataset-specific normalization and per-dataset fine-tuning, is adapted here to the joint training setting. Because PPT requires dataset labels at inference, we follow One-for-All [75] and train a lightweight dataset classifier (achieving  $\geq 95\%$  accuracy) to predict the source dataset for an input sample at test time (Sec. B.2).

**Evaluation and Implementation Details.** To ensure fair comparison, we re-benchmark PTv3 under our unified protocol by varying batch composition and normalization, which yields an average improvement of 22 mIoU (Sec. B.3). We also compare against PPT combined with One-for-All, which uses ground-truth dataset labels during training and predicted dataset labels during inference. Model capacity is denoted with -S (small) and -L (large) suffixes for all architectures, including PTv3, Point-MoE, and PPT. PTv3-S and PPT-S use 14 encoder and 8 decoder layers, while their -L variants use 18 encoder and 12 decoder layers; in contrast, both Point-MoE-S and -L have 14 encoder and 8 decoder layers, with -S using 4 experts per MoE layer and -L using 8. The expert hidden dimension is set to  $1\times$  the input dimension in Point-MoE-S and  $2\times$  in Point-MoE-L. For details, please refer to Tab. 10 in the supplementary material.

### 4.2 EXPERIMENTAL RESULTS

**Single-dataset training generalizes poorly.** We begin by evaluating the standard setting where models are trained and evaluated on individual datasets. Note that in our setup PTv3 is trained and evaluated with CLIP-guided classification in an open-set setting, consistent with the multi-dataset regime [82], whereas the original PTv3 paper reports results under standard closed-set softmax label classification [81]. This difference makes our scores not directly comparable to the numbers in the original PTv3 paper. As shown in Tab. 1a, PTv3 achieves strong results on seen datasets, but its performance drops significantly on zero-shot datasets. For instance, a PTv3 model trained on S3DIS achieves only 3.5% on Structured3D and 4.9% on ScanNet. While dataset-specific models are not expected to generalize across datasets or categories, these results underscore the brittleness of

Table 1: **Results on seen datasets.** Results are reported in mIoU. Point-MoE achieves the best average performance without using domain labels. Methods marked with \* use dataset labels during training. Models trained on a single dataset but evaluated on unseen datasets are in gray. (a) Indoor-only joint training on ScanNet [19], Structured3D [95], and S3DIS [1]. (b) Joint training across indoor and outdoor datasets: nuScenes [9] and SemanticKITTI [5].

<b>(a) Indoor-only joint training</b>									
Methods	Params	Activated	ScanNet	Structured3D	S3DIS	Avg.			
			Val	Val	Test	Area5			
<i>Single-dataset Training</i>									
PTv3-ScanNet [81]	46M	46M	75.0	19.8	20.9	8.8	31.1		
PTv3-Structured3D [81]	46M	46M	21.2	81.5	79.4	7.1	47.3		
PTv3-S3DIS [81]	46M	46M	4.9	3.5	5.3	67.6	20.3		
<i>Multi-dataset Joint Training</i>									
OA-CNNs [52]	52M	52M	71.6	59.0	58.6	60.6	62.5		
PTv3-S [81]	46M	46M	71.3	56.6	55.9	69.4	63.3		
PTv3-L [81]	97M	97M	72.2	56.0	58.1	67.4	63.4		
PPT-S* [75, 82]	47M	47M	74.7	64.2	65.5	64.7	67.3		
PPT-L* [75, 82]	98M	98M	74.8	64.7	65.9	65.0	67.6		
Point-MoE-S	59M	52M	74.5	69.0	69.9	68.0	70.4		
Point-MoE-L	100M	59M	<b>76.0</b>	<b>69.5</b>	<b>70.8</b>	<b>69.5</b>	<b>71.5</b>		

<b>(b) Indoor and Outdoor joint training</b>									
Methods	Params	Activated	ScanNet	Structured3D	S3DIS	nuScenes	SemKITTI	Avg.	
			Val	Val	Test	Area5	Val	Val	
PTv3-L [81]	97M	97M	74.6	64.1	63.9	68.0	69.6	62.9	67.2
PPT-L* [75, 82]	98M	98M	76.7	67.5	66.0	61.9	70.8	<b>66.9</b>	68.3
Point-MoE-L	100M	59M	<b>77.4</b>	<b>69.5</b>	<b>70.2</b>	<b>68.1</b>	<b>72.9</b>	66.4	<b>70.8</b>

Table 2: **Zero-shot results on unseen datasets.** Point-MoE consistently achieves the strongest generalization across unseen datasets in the zero-shot setting. Methods marked with \* use domain labels during training.

<b>(a) Indoor-only joint training</b>				<b>(b) Indoor and Outdoor joint training</b>					
Method	Matterport3D		Average	Method	Matterport3D		Waymo		Average
	Val	Test			Val	Test	Val	Test	
PTv3-L	39.0	45.4	42.2	PTv3-L	39.1	45.9	21.9	23.2	32.5
PPT-L*	27.8	26.3	27.1	PPT-L*	24.9	23.1	16.3	16.7	20.3
Point-MoE-L	<b>41.0</b>	<b>46.7</b>	<b>43.9</b>	Point-MoE-L	<b>41.3</b>	<b>49.6</b>	<b>23.7</b>	<b>25.3</b>	<b>35.0</b>

single-dataset training. This motivates the need for multi-dataset joint training strategies that expose the model to diverse data and promote broader generalization.

**Point-MoE surpasses all baselines on seen datasets, without dataset labels during training.**

Point-MoE dispenses with dataset identifiers during training yet yields consistent gains across indoor benchmarks (Tab. 1a); both Point-MoE-S and Point-MoE-L variants improve on ScanNet, Structured3D, and S3DIS, with Point-MoE-L attaining a new state-of-the-art average of 71.5 mIoU. Despite joint training over multiple datasets, Point-MoE matches or exceeds single-dataset specialists, indicating effective expert routing rather than overfitting to any one source, or significantly exhibiting the negative transfer effects noted in PPT [82]. In the more challenging indoor and outdoor joint training setting (Tab. 1b), Point-MoE maintains its advantage across datasets and, on average, surpasses PTv3-L by 3.55 mIoU and PPT-L by 2.45 mIoU, demonstrating that label-free expert routing scales to heterogeneous datasets while simplifying the training pipeline. Moreover, performance on the seen indoor datasets remains closely aligned between indoor-only training and indoor-outdoor joint training, suggesting that Point-MoE preserves seen datasets accuracy even when subsequently trained jointly with outdoor data. This generalization is achieved implicitly in the model, without requiring dataset labels for incoming samples or maintaining explicit per-dataset normalization parameters. Note, since we use a lightweight dataset classifier, PPT’s performance differs from what is reported

Table 3: **Ablations of Point-MoE designs and hyperparameters.** We conduct a systematic ablation on key design and hyperparameter choices of Point-MoE across four indoor multi-domain datasets: ScanNet (Scan), Structured3D (S3D), S3DIS, and Matterport3D (Mat).

$\alpha$	Scan	S3D	S3DIS	Mat	top $k$	Scan	S3D	S3DIS	Mat	norm	Scan	S3D	S3DIS	Mat
0	<b>74.5</b>	<b>66.9</b>	<b>68.6</b>	<b>40.1</b>	top 1	74.4	64.8	65.5	39.0	BN.	<b>74.5</b>	<b>66.9</b>	<b>68.6</b>	<b>40.1</b>
$10^{-4}$	72.3	64.1	67.9	39.5	top 2	<b>74.5</b>	<b>66.9</b>	<b>68.6</b>	<b>40.1</b>	LN.	70.8	56.9	67.3	37.2
$10^{-3}$	71.6	58.8	67.4	37.4	top 3	73.8	62.4	67.8	39.7	RMS.	45.3	36.5	51.1	24.6
(a) <b>Auxiliary load balancing loss.</b> Removing the auxiliary loss consistently improves performance.					(b) <b>Top-<math>k</math> expert selection.</b> Best performance is achieved with $k=2$ experts across datasets.					(c) <b>Normalization.</b> BatchNorm yields strongest performance; RMSNorm degrades results.				
case	Scan	S3D	S3DIS	Mat	act.	Scan	S3D	S3DIS	Mat	case	Scan	S3D	S3DIS	Mat
FFN	72.6	66.1	66.9	39.2	SiLU	73.6	65.7	64.9	<b>40.1</b>	1H	73.0	<b>60.3</b>	<b>66.3</b>	39.5
Proj.	<b>74.5</b>	<b>66.9</b>	<b>68.6</b>	<b>40.1</b>	ReLU	<b>74.5</b>	<b>66.9</b>	<b>68.6</b>	<b>40.1</b>	2H	<b>73.5</b>	58.6	65.4	<b>39.8</b>
(d) <b>MoE position.</b> Replacing the projection layer performs better.					(e) <b>Activation functions.</b> ReLU performs the best.					(f) <b>Expert width.</b> H indicates original feature dimension.				
shared	Scan	S3D	S3DIS	Mat	num.	Scan	S3D	S3DIS	Mat	batch	Scan	S3D	S3DIS	Mat
0	<b>74.5</b>	<b>66.9</b>	<b>68.6</b>	<b>40.1</b>	4	<b>74.5</b>	66.9	<b>68.5</b>	40.1	4	74.0	64.9	66.6	38.1
1	73.6	62.3	66.6	39.1	8	73.6	<b>68.7</b>	<b>68.5</b>	<b>40.4</b>	6	<b>74.3</b>	<b>66.9</b>	<b>68.6</b>	<b>40.1</b>
(g) <b>Shared experts.</b> Not sharing experts yields better performance.					(h) <b>Number of experts.</b> More experts improve performance.					(i) <b>Batch size.</b> Larger batchsize improves performance.				

in the original paper, where oracle dataset identifiers are provided at inference. Finally, because only a subset of experts is activated, Point-MoE achieves a favorable accuracy–compute trade-off, cutting compute by 30.9% (265.7 vs. 384.4 GFLOPs) and peak VRAM by 19.0% (33.3 vs. 41.1 GiB) relative to PPT-L (Tab. 5). We analyze the emergent dataset-awareness and routing behavior in Sec. 4.4.

**Point-MoE outperforms all baselines consistently across zero-shot datasets.** As shown in Tab. 2a and Tab. 2b, Point-MoE-L achieves the strongest zero shot performance, including on Matterport3D under indoor only training and on both Matterport3D and Waymo under indoor and outdoor training, without using dataset labels during training. We believe a key reason is that label free expert routing encourages specialization based on the underlying semantics and geometry of the input rather than on dataset identity, resulting in more stable behavior under distribution shift. By contrast, PPT-L relies on explicit dataset labels during training. While this provides useful supervision on seen datasets, it can also encourage the model to depend too heavily on dataset specific cues. As a result, when a dataset is held out and its label is unavailable or no longer aligned with the training distribution at test time, this dependence becomes brittle and can hurt generalization. Additional analysis of Point-MoE’s zero shot adaptation is provided in Sec. 4.4.

### 4.3 MOE DESIGN ABLATION

We investigate the impact of MoE design choices and hyper-parameters choices in indoor multi-dataset 3D semantic segmentation. Results are presented in Tab. 3. Note we are not using precise evaluator so results are not directly comparable to Tab. 1. Please refer to details in Sec. B.3 in the supplementary material.

**Effect of load-balancing loss.** The auxiliary load-balancing loss is designed to encourage uniform expert usage and prevent expert collapse [42, 56, 78]. We ablate its effect by training models with varying strengths of this loss in Tab. 3a. Interestingly, we find that removing the auxiliary loss entirely leads to consistently better performance across datasets. In contrast, stronger auxiliary losses result in significant degradation. We hypothesize that this is due to the inherent imbalance in the distribution of samples across datasets in 3D point cloud datasets—a phenomenon also observed by ChartMoE [87].

**Effect of activated experts.** Tab. 3b compares the performance of configurations with 1, 2 and 3 activated experts, finding diminishing return when increasing number of activated experts. We find that activating two experts yields the best performance across datasets. This analysis suggests that merely increasing the number of activated experts does not guarantee improved performance.

**Effect of MoE position.** We compare placing MoE in the feed-forward network (FFN) versus in the attention output projection  $W_o$ , holding all other components fixed. Projection-MoE consistently outperforms FFN-MoE in Tab. 3d. We hypothesize that  $W_o$  is the fusion point where multi-head outputs are recombined *before* the next normalization, so experts placed there can route on richer, head-aggregated signals that preserve cross-dataset geometry cues, while leaving  $W_q, W_k, W_v$  shared and stable; in contrast, FFN experts operate on post-normalized activations where such dataset or geometry cues are more attenuated. This empirical gain leads us to adopt projection-MoE as the default. Similar observations also appear in recent work: *e.g.* UMoE [89] finds that using MoE for the output (and value) projections yields strong compute savings with high performance.

**Effect of model scaling with MoE.** Tab. 3h compares Point-MoE with 4 and 8 experts with activated experts fixed at 2. Increasing the number of experts from 4 to 8 leads to improved performance on seen and zero-shot datasets. Tab. 3f ablates the expert width by varying the intermediate feature dimension and the results show a mixed trend: wider experts improve performance on ScanNet and Matterport3D, but degrade results on Structured3D and S3DIS. Finally, we investigate the effect of adding shared experts [20, 65, 73]. We find that disabling shared experts consistently leads to better accuracy and dataset specialization across all benchmarks, as reported in Tab. 3g.

**Effect of hyper-parameter choices.** We provide justification for our selected hyper-parameters. In Tab. 3c, BatchNorm [29] consistently outperforms other normalization methods [3, 91] in the multi-datasets setting. Tab. 3e shows that ReLU [50] slightly outperforms SiLU [23]. Additionally, Tab. 3i demonstrates that importance of batch size in MoE training. In general, larger batch sizes lead to improved performance across datasets.

**Mixed dataset training.** In joint multi-dataset training, forming each minibatch with samples drawn from multiple datasets is consistently beneficial. Although there is no explicit batch-level interaction module, samples from different datasets still influence one another through shared normalization statistics and, for Point-MoE, through competition over a common expert pool. As shown in Tab. 4, this *mixed-dataset training* strategy improves the average mIoU of all backbones: PTV3 +8.3, PPT +2.9, and Point-MoE +16.6 mIoU on average. For dense backbones such as PTV3 and PPT, mixing exposes the model to more diverse domain statistics within each optimization step, which appears to regularize training and reduce overfitting to dataset-specific feature distributions. To make this comparison fair for PPT, we re-implemented its normalization module so that mixed-dataset batching is supported. The effect is most pronounced for Point-MoE, where diverse minibatches promote expert specialization across datasets, stabilizing routing and improving generalization.

Table 4: **Ablations for mixed-dataset training.** “Mix” indicates that each training batch combines samples from multiple datasets.

Methods	Mix	Scan	S3D	S3DIS	Mat	Average
PTv3		48.4	<b>57.8</b>	44.1	27.8	44.5
PTv3	✓	<b>67.7</b>	45.9	<b>62.5</b>	<b>34.9</b>	<b>52.8</b> (+8.3)
PPT		74.2	58.2	61.0	24.3	54.4
PPT	✓	<b>74.4</b>	<b>61.4</b>	<b>62.1</b>	<b>31.1</b>	<b>57.3</b> (+2.9)
PT-MoE		54.1	60.9	40.6	28.0	45.9
PT-MoE	✓	<b>74.5</b>	<b>66.9</b>	<b>68.6</b>	<b>40.1</b>	<b>62.5</b> (+16.6)

#### 4.4 ANALYSIS OF MOE

**Dataset clustering emerges in Point-MoE.** Fig. 2 shows t-SNE visualizations [70] of encoder and decoder features from PTV3, PPT [82], and Point-MoE. PTV3 exhibits no clear separation in either space, indicating limited capacity to form dataset-specific representations. PPT, by contrast, produces sharply separated clusters at both encoder and decoder levels, reflecting its reliance on dataset labels during training. While this aids seen-datasets performance, such rigid partitioning may hinder generalization capabilities as highlighted in Tab. 2. Point-MoE displays a different pattern: encoder features remain mixed across datasets, supporting shared representation learning, while the decoder disentangles dataset-specific structures. This apparent division of labor suggests that Point-MoE performs implicit dataset inference, without requiring explicit labels. Crucially, on the zero-shot Matterport3D dataset, Point-MoE aligns samples with the most related seen-dataset clusters (*e.g.*, ScanNet), which likely contributes to its strong generalization. Overall, these results show that Point-MoE can self-organize its experts and adapt to novel environments by effectively transferring knowledge across diverse training datasets.

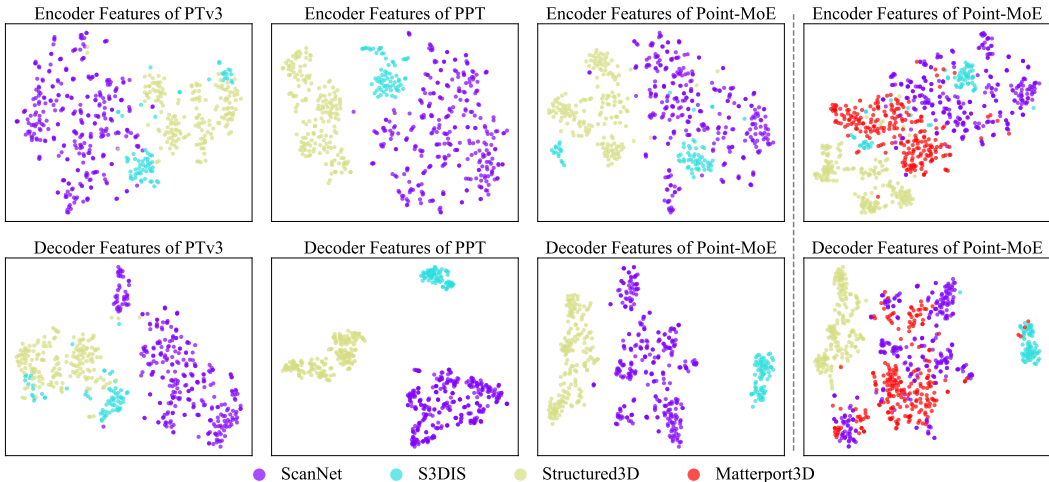


Figure 2: **t-SNE visualization of feature clustering.** The first three columns show that the decoders of both PPT and PointMoE have better separation between datasets in their decoder representations, than vanilla PTv3. The rightmost column highlights how Point-MoE generalizes to zero-shot datasets, with Matterport3D features aligning closely with ScanNet, which is indeed semantically similar.

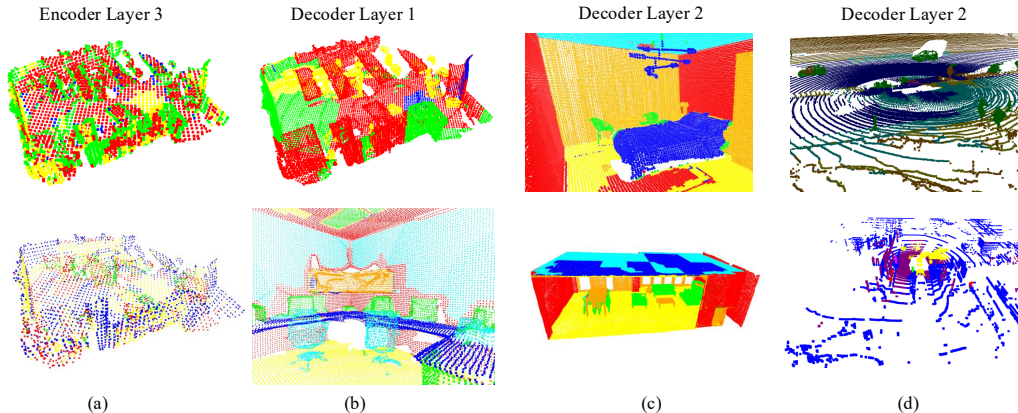


Figure 3: **Expert choice visualization.** Different colors within each image indicate different experts, showing that Point-MoE self-organizes point routing based on spatial and semantic cues across different layers. (a) shows one expert (green) focusing on edges, suggesting spatially aware mid-level routing in the encoder. (b) and (c) show that semantically related regions (*e.g.*, chairs and desks) are consistently assigned to the same expert, even across datasets. (d) shows meaningful routing in an outdoor scene with sparse LiDAR points despite lower point density and more irregular geometry.

**Expert choice visualization.** Fig. 3 visualizes expert assignments for validation scenes at selected encoder and decoder layers. In (a), the encoder layer primarily routes points according to local geometric structure. In particular, one expert (green) is consistently activated around object boundaries and thin structural regions, such as the edges of desks and chairs, while other experts dominate flatter surfaces, suggesting spatially aware mid-level routing in the encoder. In (b) and (c), the decoder layers exhibit more semantically coherent expert selection. Semantically related regions, such as chairs, desks, floors, and walls, are more consistently assigned to the same experts, even across different scenes and datasets, likely because decoder features are closer to the supervision signal and thus encode higher-level semantics. In (d), we examine an outdoor scene with sparse LiDAR points. Despite the lower point density and more irregular geometry, the model still produces meaningful routing patterns rather than random assignments. Nearby foreground regions and farther background regions tend to activate different experts, suggesting that the learned routing generalizes beyond dense indoor scans to more challenging outdoor environments. Additional visualizations are provided in Sec. C.3. We also observe a few isolated points assigned to different experts than their neighbors, possibly due to PTv3 design choices such as point serialization and positional encoding.

Table 5: **Inference efficiency.** FLOPs per step are measured with a profiler, and peak VRAM reports *allocated* memory. Relative deltas are computed with respect to PPT-L.

Model	FLOPs/step (GFLOPs)	Peak VRAM (GiB)	$\Delta$ FLOPs vs. PPT-L	$\Delta$ VRAM vs. PPT-L
PPT-L	384.4	41.1	0%	0%
PTv3	375.8	37.4	↓ 2.2%	↓ 9.0%
Point-MoE-L	265.7	33.3	↓ 30.9%	↓ 19.0%

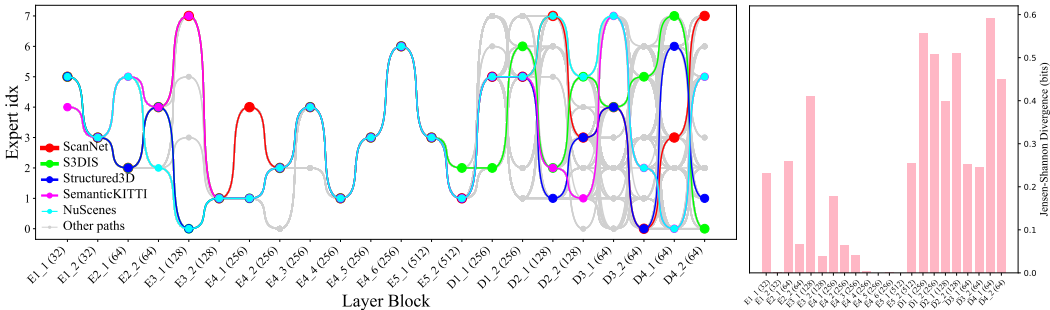


Figure 4: **Expert routing across datasets.** *Left:* the most frequent expert paths through each encoder (E) and decoder (D) layer, with channel sizes in parentheses, showing that expert selection varies across datasets. The effect is especially pronounced in decoder MoE layers. *Right:* Jensen Shannon Divergence (JSD) between dataset specific expert selection distributions at each MoE layer.

**Token pathways.** To understand how Point-MoE adapts to diverse datasets, we analyze expert routing at the token level. We track each token’s top-1 expert across all MoE layers and reconstruct full routing trajectories from the final layer back to the first. We then rank expert paths by frequency and focus on the top 100 (Fig. 4). Encoder paths are notably less diverse than decoder paths, suggesting that encoders perform more dataset-agnostic processing. We also find sparse routing in deeper encoder layers, likely due not to feature reuse but to the U-Net design: features grow deeper spatially while tokens become sparser, reducing routing variability. When examining dataset-level trends, we find that certain dataset pairs, such as SemanticKITTI and nuScenes or ScanNet and Structured3D, share similar expert pathways, suggesting that Point-MoE implicitly clusters datasets with related geometric or semantic structures. To quantify these observations, we compute the Jensen-Shannon Divergence (JSD) [45] between expert selection distributions across datasets at each MoE layer. JSD [45] is an entropy-based measure of divergence between expert routing distributions across datasets, weighted by their token proportions; its formal definition is provided in the supplementary. As shown in Fig. 4 (right), decoder layers exhibit significantly higher JSD, indicating stronger dataset-specific specialization. Several encoder layers also display nontrivial JSD, underscoring the benefit of placing MoE throughout the network (see Sec. C.2 for more analysis).

**Efficiency analysis.** As shown in Tab. 5, Point-MoE-L requires only 265.7 GFLOPs per step and 33.3 GiB peak VRAM, reducing compute by 30.9% and memory by 19.0% relative to PPT-L (384.4 GFLOPs and 41.1 GiB). It is also more efficient than PTv3 (375.8 GFLOPs and 37.4 GiB). Despite this lower cost, Point-MoE-L achieves the best average mIoU in both settings, reaching 71.5 in indoor only joint training and 70.2 in indoor and outdoor joint training (Tab. 1).

## 5 DISCUSSIONS

This work embraces the “bitter lesson” [68] in AI: scalable generalization emerges from flexible architectures trained on diverse data, rather than hand-engineered domain priors. We introduce Point-MoE, a mixture-of-experts architecture for 3D understanding that dynamically routes tokens to specialized experts across both indoor and outdoor domains. Our experiments demonstrate that Point-MoE not only achieves superior performance on seen datasets but also generalizes effectively to zero-shot datasets without explicit domain labels. Through careful analysis of expert routing behavior, we show that the model self-organizes around both geometric and semantic structures, adapting its computation pathways to the nature of the input. These results highlight the potential of sparse, modular computation for robust and scalable 3D scene understanding. We provide more analysis of Point-MoE and discuss our limitations in the supplementary materials.

## 6 ACKNOWLEDGEMENT

The authors acknowledge the MathWorks Research Award, Adobe Research Gift, the University of Virginia Research Computing and Data Analytics Center, Advanced Micro Devices AI and HPC Cluster Program, Advanced Cyberinfrastructure Coordination Ecosystem: Services & Support (ACCESS) program, and National Artificial Intelligence Research Resource (NAIRR) Pilot for computational resources, including the Anvil supercomputer (National Science Foundation award OAC 2005632) at Purdue University and the Delta and DeltaAI advanced computing resources (National Science Foundation award OAC 2005572).

## REFERENCES

- [1] Iro Armeni, Ozan Sener, Amir R. Zamir, Helen Jiang, Ioannis Brilakis, Martin Fischer, and Silvio Savarese. 3d semantic parsing of large-scale indoor spaces. In *2016 IEEE Conference on Computer Vision and Pattern Recognition (CVPR)*, pp. 1534–1543, 2016. doi: 10.1109/CVPR.2016.170. [5](#), [6](#), [18](#), [19](#), [21](#)
- [2] Armen Avetisyan, Christopher Xie, Henry Howard-Jenkins, Tsun-Yi Yang, Samir Aroudj, Suvam Patra, Fuyang Zhang, Duncan Frost, Luke Holland, Campbell Orme, et al. Scenescrypt: Reconstructing scenes with an autoregressive structured language model. In *European Conference on Computer Vision*, pp. 247–263. Springer, 2024. [1](#)
- [3] Jimmy Lei Ba, Jamie Ryan Kiros, and Geoffrey E Hinton. Layer normalization. *arXiv preprint arXiv:1607.06450*, 2016. [8](#), [22](#)
- [4] Max Bain, Arsha Nagrani, Gül Varol, and Andrew Zisserman. Frozen in time: A joint video and image encoder for end-to-end retrieval. In *IEEE International Conference on Computer Vision*, 2021. [1](#)
- [5] J. Behley, M. Garbade, A. Milioto, J. Quenzel, S. Behnke, C. Stachniss, and J. Gall. SemanticKITTI: A Dataset for Semantic Scene Understanding of LiDAR Sequences. In *Proc. of the IEEE/CVF International Conf. on Computer Vision (ICCV)*, 2019. [1](#), [5](#), [6](#), [18](#), [19](#), [21](#), [30](#)
- [6] Bruce Blumberg et al. Precise workcell sketching from point clouds using an ar toolbox. *arXiv preprint arXiv:2410.00479*, 2024. [1](#)
- [7] Tom Brown, Benjamin Mann, Nick Ryder, Melanie Subbiah, Jared D Kaplan, Prafulla Dhariwal, Arvind Neelakantan, Pranav Shyam, Girish Sastry, Amanda Askell, et al. Language models are few-shot learners. *Advances in neural information processing systems*, 33:1877–1901, 2020. [1](#)
- [8] Minwoo Byeon, Beomhee Park, Haecheon Kim, Sungjun Lee, Woonhyuk Baek, and Sae-hoon Kim. Coyo-700m: Image-text pair dataset. <https://github.com/kakaobrain/coyo-dataset>, 2022. [1](#)
- [9] Holger Caesar, Varun Bankiti, Alex H Lang, Sourabh Vora, Venice Erin Liong, Qiang Xu, Anush Krishnan, Yu Pan, Giancarlo Baldan, and Oscar Beijbom. nuscenes: A multimodal dataset for autonomous driving. In *Proceedings of the IEEE/CVF conference on computer vision and pattern recognition*, pp. 11621–11631, 2020. [1](#), [5](#), [6](#), [18](#), [19](#), [21](#), [30](#)
- [10] Angel Chang, Angela Dai, Thomas Funkhouser, Maciej Halber, Matthias Niessner, Manolis Savva, Shuran Song, Andy Zeng, and Yinda Zhang. Matterport3d: Learning from rgb-d data in indoor environments. *arXiv preprint arXiv:1709.06158*, 2017. [5](#), [18](#), [19](#), [30](#)
- [11] Shizhe Chen, Ricardo Garcia, Cordelia Schmid, and Ivan Laptev. Polarnet: 3d point clouds for language-guided robotic manipulation. *arXiv preprint arXiv:2309.15596*, 2023. [1](#)
- [12] Siheng Chen, Baoan Liu, Chen Feng, Carlos Vallespi-Gonzalez, and Carl Wellington. 3d point cloud processing and learning for autonomous driving. *arXiv preprint arXiv:2003.00601*, 2020. [1](#)
- [13] Xiaozhi Chen, Huimin Ma, Ji Wan, Bo Li, and Tian Xia. Multi-view 3d object detection network for autonomous driving. In *Proceedings of the IEEE conference on Computer Vision and Pattern Recognition*, pp. 1907–1915, 2017. [1](#), [3](#)

- [14] Zitian Chen, Yikang Shen, Mingyu Ding, Zhenfang Chen, Hengshuang Zhao, Erik G Learned-Miller, and Chuang Gan. Mod-squad: Designing mixtures of experts as modular multi-task learners. In *Proceedings of the IEEE/CVF Conference on Computer Vision and Pattern Recognition*, pp. 11828–11837, 2023. 3
- [15] Nadezhda Chirkova, Vassilina Nikoulina, Jean-Luc Meunier, and Alexandre Bérard. Investigating the potential of sparse mixtures-of-experts for multi-domain neural machine translation. *arXiv preprint arXiv:2407.01126*, 2024. 2, 3
- [16] Aakanksha Chowdhery, Sharan Narang, Jacob Devlin, Maarten Bosma, Gaurav Mishra, Adam Roberts, Paul Barham, Hyung Won Chung, Charles Sutton, Sebastian Gehrmann, et al. Palm: Scaling language modeling with pathways. *Journal of Machine Learning Research*, 24(240): 1–113, 2023. 1
- [17] Christopher Choy, JunYoung Gwak, and Silvio Savarese. 4d spatio-temporal convnets: Minkowski convolutional neural networks. In *Proceedings of the IEEE/CVF conference on computer vision and pattern recognition*, pp. 3075–3084, 2019. 3
- [18] Pointcept Contributors. Pointcept: A codebase for point cloud perception research. <https://github.com/Pointcept/Pointcept>, 2023. 19, 21
- [19] Angela Dai, Angel X Chang, Manolis Savva, Maciej Halber, Thomas Funkhouser, and Matthias Nießner. Scannet: Richly-annotated 3d reconstructions of indoor scenes. In *Proceedings of the IEEE conference on computer vision and pattern recognition*, pp. 5828–5839, 2017. 1, 5, 6, 18, 19, 21, 30
- [20] Damai Dai, Chengqi Deng, Chenggang Zhao, RX Xu, Huazuo Gao, Deli Chen, Jiashi Li, Wangding Zeng, Xingkai Yu, Yu Wu, et al. Deepseekmoe: Towards ultimate expert specialization in mixture-of-experts language models. *arXiv preprint arXiv:2401.06066*, 2024. 2, 3, 8
- [21] Alexey Dosovitskiy, Lucas Beyer, Alexander Kolesnikov, Dirk Weissenborn, Xiaohua Zhai, Thomas Unterthiner, Mostafa Dehghani, Matthias Minderer, Georg Heigold, Sylvain Gelly, et al. An image is worth 16x16 words: Transformers for image recognition at scale. *arXiv preprint arXiv:2010.11929*, 2020. 1
- [22] Nan Du, Yanping Huang, Andrew M Dai, Simon Tong, Dmitry Lepikhin, Yuanzhong Xu, Maxim Krikun, Yanqi Zhou, Adams Wei Yu, Orhan Firat, et al. Glam: Efficient scaling of language models with mixture-of-experts. In *International conference on machine learning*, pp. 5547–5569. PMLR, 2022. 2, 3
- [23] Stefan Elfving, Eiji Uchibe, and Kenji Doya. Sigmoid-weighted linear units for neural network function approximation in reinforcement learning. *Neural networks*, 107:3–11, 2018. 8
- [24] William Fedus, Barret Zoph, and Noam Shazeer. Switch transformers: Scaling to trillion parameter models with simple and efficient sparsity. *Journal of Machine Learning Research*, 23(120):1–39, 2022. 2, 3
- [25] Benjamin Graham, Martin Engelcke, and Laurens Van Der Maaten. 3d semantic segmentation with submanifold sparse convolutional networks. In *Proceedings of the IEEE conference on computer vision and pattern recognition*, pp. 9224–9232, 2018. 3
- [26] Jiang Guo, Darsh J Shah, and Regina Barzilay. Multi-source domain adaptation with mixture of experts. *arXiv preprint arXiv:1809.02256*, 2018. 3
- [27] Meng-Hao Guo, Jun-Xiong Cai, Zheng-Ning Liu, Tai-Jiang Mu, Ralph R. Martin, and Shi-Min Hu. Pct: Point cloud transformer. *Computational Visual Media*, 7(2):187–199, June 2021. ISSN 2096-0662. doi: 10.1007/s41095-021-0229-5. URL <http://dx.doi.org/10.1007/s41095-021-0229-5>. 3
- [28] Suchin Gururangan, Mike Lewis, Ari Holtzman, Noah A Smith, and Luke Zettlemoyer. Demix layers: Disentangling domains for modular language modeling. *arXiv preprint arXiv:2108.05036*, 2021. 3

- [29] Sergey Ioffe and Christian Szegedy. Batch normalization: Accelerating deep network training by reducing internal covariate shift. In *International conference on machine learning*, pp. 448–456. pmlr, 2015. 8
- [30] Robert A. Jacobs, Michael I. Jordan, Steven J. Nowlan, and Geoffrey E. Hinton. Adaptive mixtures of local experts. *Neural Computation*, 3(1):79–87, 1991. doi: 10.1162/neco.1991.3.1.79. 2, 3, 4
- [31] Yash Jain, Harkirat Behl, Zsolt Kira, and Vibhav Vineet. Damex: Dataset-aware mixture-of-experts for visual understanding of mixture-of-datasets. *Advances in Neural Information Processing Systems*, 36:69625–69637, 2023. 3
- [32] Guangda Ji, Silvan Weder, Francis Engelmann, Marc Pollefeys, and Hermann Blum. Arkit labelmaker: A new scale for indoor 3d scene understanding. In *Proceedings of the Computer Vision and Pattern Recognition Conference*, pp. 4398–4407, 2025. 3
- [33] Albert Q Jiang, Alexandre Sablayrolles, Antoine Roux, Arthur Mensch, Blanche Savary, Chris Bamford, Devendra Singh Chaplot, Diego de las Casas, Emma Bou Hanna, Florian Bressand, et al. Mixtral of experts. *arXiv preprint arXiv:2401.04088*, 2024. 3
- [34] M.I. Jordan and R.A. Jacobs. Hierarchical mixtures of experts and the em algorithm. In *Proceedings of 1993 International Conference on Neural Networks (IJCNN-93-Nagoya, Japan)*, volume 2, pp. 1339–1344 vol.2, 1993. doi: 10.1109/IJCNN.1993.716791. 2, 3
- [35] Hyeonseong Kim, Yoonsu Kang, Changgyoon Oh, and Kuk-Jin Yoon. Single domain generalization for lidar semantic segmentation. In *Proceedings of the IEEE/CVF conference on computer vision and pattern recognition*, pp. 17587–17598, 2023. 3
- [36] Alexander Kirillov, Eric Mintun, Nikhila Ravi, Hanzi Mao, Chloe Rolland, Laura Gustafson, Tete Xiao, Spencer Whitehead, Alexander C Berg, Wan-Yen Lo, et al. Segment anything. In *Proceedings of the IEEE/CVF international conference on computer vision*, pp. 4015–4026, 2023. 1
- [37] Maksim Kolodiazny, Anna Vorontsova, Matvey Skripkin, Danila Rukhovich, and Anton Konushin. Unidet3d: Multi-dataset indoor 3d object detection. In *Proceedings of the AAAI Conference on Artificial Intelligence*, volume 39, pp. 4365–4373, 2025. 3
- [38] Alex H Lang, Sourabh Vora, Holger Caesar, Lubing Zhou, Jiong Yang, and Oscar Beijbom. Pointpillars: Fast encoders for object detection from point clouds. In *Proceedings of the IEEE/CVF conference on computer vision and pattern recognition*, pp. 12697–12705, 2019. 3
- [39] Junha Lee, Chunghyun Park, Jaesung Choe, Yu-Chiang Frank Wang, Jan Kautz, Minsu Cho, and Chris Choy. Mosaic3d: Foundation dataset and model for open-vocabulary 3d segmentation. In *Proceedings of the Computer Vision and Pattern Recognition Conference*, pp. 14089–14101, 2025. 3
- [40] Dmitry Lepikhin, HyoukJoong Lee, Yuanzhong Xu, Dehao Chen, Orhan Firat, Yanping Huang, Maxim Krikun, Noam Shazeer, and Zhifeng Chen. Gshard: Scaling giant models with conditional computation and automatic sharding. *arXiv preprint arXiv:2006.16668*, 2020. 2, 3
- [41] Bo Li, Tianlei Zhang, and Tian Xia. Vehicle detection from 3d lidar using fully convolutional network. *arXiv preprint arXiv:1608.07916*, 2016. 3
- [42] Dengchun Li, Yingzi Ma, Naizheng Wang, Zhengmao Ye, Zhiyuan Cheng, Yinghao Tang, Yan Zhang, Lei Duan, Jie Zuo, Cal Yang, et al. Mixlora: Enhancing large language models fine-tuning with lora-based mixture of experts. *arXiv preprint arXiv:2404.15159*, 2024. 7
- [43] Ying Li, Lingfei Ma, Zilong Zhong, Fei Liu, Michael A Chapman, Dongpu Cao, and Jonathan Li. Deep learning for lidar point clouds in autonomous driving: A review. *IEEE Transactions on Neural Networks and Learning Systems*, 32(8):3412–3432, 2020. 1

- [44] Bin Lin, Zhenyu Tang, Yang Ye, Jiayi Cui, Bin Zhu, Peng Jin, Jinfa Huang, Junwu Zhang, Yatian Pang, Munan Ning, et al. Moe-llava: Mixture of experts for large vision-language models. *arXiv preprint arXiv:2401.15947*, 2024. 3
- [45] Jianhua Lin. Divergence measures based on the shannon entropy. *IEEE Trans. Inf. Theory*, 37:145–151, 1991. URL <https://api.semanticscholar.org/CorpusID:12121632>. 10
- [46] Aixin Liu, Bei Feng, Bin Wang, Bingxuan Wang, Bo Liu, Chenggang Zhao, Chengqi Deng, Chong Ruan, Damai Dai, Daya Guo, et al. Deepseek-v2: A strong, economical, and efficient mixture-of-experts language model. *arXiv preprint arXiv:2405.04434*, 2024. 3
- [47] Aixin Liu, Bei Feng, Bing Xue, Bingxuan Wang, Bochao Wu, Chengda Lu, Chenggang Zhao, Chengqi Deng, Chenyu Zhang, Chong Ruan, et al. Deepseek-v3 technical report. *arXiv preprint arXiv:2412.19437*, 2024. 3, 5
- [48] Haoyu Lu, Wen Liu, Bo Zhang, Bingxuan Wang, Kai Dong, Bo Liu, Jingxiang Sun, Tongzheng Ren, Zhuoshu Li, Hao Yang, et al. Deepseek-v1: towards real-world vision-language understanding. *arXiv preprint arXiv:2403.05525*, 2024. 3
- [49] Daniel Maturana and Sebastian Scherer. Voxnet: A 3d convolutional neural network for real-time object recognition. In *2015 IEEE/RSJ International Conference on Intelligent Robots and Systems (IROS)*, pp. 922–928, 2015. doi: 10.1109/IROS.2015.7353481. 3
- [50] Vinod Nair and Geoffrey E Hinton. Rectified linear units improve restricted boltzmann machines. In *Proceedings of the 27th international conference on machine learning (ICML-10)*, pp. 807–814, 2010. 8
- [51] Maxime Oquab, Timothée Darcet, Théo Moutakanni, Huy Vo, Marc Szafraniec, Vasil Khalidov, Pierre Fernandez, Daniel Haziza, Francisco Massa, Alaaeldin El-Nouby, et al. Dinov2: Learning robust visual features without supervision. *arXiv preprint arXiv:2304.07193*, 2023. 1
- [52] Bohao Peng, Xiaoyang Wu, Li Jiang, Yukang Chen, Hengshuang Zhao, Zhuotao Tian, and Jiaya Jia. Oa-cnns: Omni-adaptive sparse cnns for 3d semantic segmentation. In *Proceedings of the IEEE/CVF Conference on Computer Vision and Pattern Recognition*, pp. 21305–21315, 2024. 5, 6, 20
- [53] Skand Peri, Iain Lee, Chanho Kim, Li Fuxin, Tucker Hermans, and Stefan Lee. Point cloud models improve visual robustness in robotic learners. In *2024 IEEE International Conference on Robotics and Automation (ICRA)*, pp. 17529–17536. IEEE, 2024. 1
- [54] Charles R Qi, Hao Su, Kaichun Mo, and Leonidas J Guibas. Pointnet: Deep learning on point sets for 3d classification and segmentation. In *Proceedings of the IEEE conference on computer vision and pattern recognition*, pp. 652–660, 2017. 3
- [55] Charles Ruizhongtai Qi, Li Yi, Hao Su, and Leonidas J Guibas. Pointnet++: Deep hierarchical feature learning on point sets in a metric space. *Advances in neural information processing systems*, 30, 2017. 3
- [56] Zihan Qiu, Zeyu Huang, Bo Zheng, Kaiyue Wen, Zekun Wang, Rui Men, Ivan Titov, Dayiheng Liu, Jingren Zhou, and Junyang Lin. Demons in the detail: On implementing load balancing loss for training specialized mixture-of-expert models. *arXiv preprint arXiv:2501.11873*, 2025. 7
- [57] Alec Radford, Jong Wook Kim, Chris Hallacy, Aditya Ramesh, Gabriel Goh, Sandhini Agarwal, Girish Sastry, Amanda Askell, Pamela Mishkin, Jack Clark, et al. Learning transferable visual models from natural language supervision. In *International conference on machine learning*, pp. 8748–8763. PmLR, 2021. 1, 4
- [58] Colin Raffel, Noam Shazeer, Adam Roberts, Katherine Lee, Sharan Narang, Michael Matena, Yanqi Zhou, Wei Li, and Peter J Liu. Exploring the limits of transfer learning with a unified text-to-text transformer. *Journal of machine learning research*, 21(140):1–67, 2020. 1

- [59] Carlos Riquelme, Joan Puigcerver, Basil Mustafa, Maxim Neumann, Rodolphe Jenatton, André Susano Pinto, Daniel Keysers, and Neil Houlsby. Scaling vision with sparse mixture of experts. *Advances in Neural Information Processing Systems*, 34:8583–8595, 2021. 2, 3
- [60] Cristiano Saltori, Aljosa Osep, Elisa Ricci, and Laura Leal-Taixé. Walking your lidog: A journey through multiple domains for lidar semantic segmentation. In *Proceedings of the IEEE/CVF international conference on computer vision*, pp. 196–206, 2023. 3
- [61] Christoph Schuhmann, Romain Beaumont, Richard Vencu, Cade Gordon, Ross Wightman, Mehdi Cherti, Theo Coombes, Aarush Katta, Clayton Mullis, Mitchell Wortsman, et al. Laion-5b: An open large-scale dataset for training next generation image-text models. *Advances in neural information processing systems*, 35:25278–25294, 2022. 1
- [62] Noam Shazeer, Azalia Mirhoseini, Krzysztof Maziarz, Andy Davis, Quoc Le, Geoffrey Hinton, and Jeff Dean. Outrageously large neural networks: The sparsely-gated mixture-of-experts layer. *arXiv preprint arXiv:1701.06538*, 2017. 3
- [63] Shuran Song, Fisher Yu, Andy Zeng, Angel X Chang, Manolis Savva, and Thomas Funkhouser. Semantic scene completion from a single depth image. In *Proceedings of the IEEE conference on computer vision and pattern recognition*, pp. 1746–1754, 2017. 3
- [64] Hang Su, Subhransu Maji, Evangelos Kalogerakis, and Erik Learned-Miller. Multi-view convolutional neural networks for 3d shape recognition. In *Proceedings of the IEEE international conference on computer vision*, pp. 945–953, 2015. 3
- [65] Zhenpeng Su, Xing Wu, Zijia Lin, Yizhe Xiong, Minxuan Lv, Guangyuan Ma, Hui Chen, Songlin Hu, and Guiguang Ding. Cartesianmoe: Boosting knowledge sharing among experts via cartesian product routing in mixture-of-experts. *arXiv preprint arXiv:2410.16077*, 2024. 8
- [66] Chen Sun, Abhinav Shrivastava, Saurabh Singh, and Abhinav Gupta. Revisiting unreasonable effectiveness of data in deep learning era. In *Proceedings of the IEEE international conference on computer vision*, pp. 843–852, 2017. 1
- [67] Pei Sun, Henrik Kretschmar, Xerxes Dotiwalla, Aurelien Chouard, Vijaysai Patnaik, Paul Tsui, James Guo, Yin Zhou, Yuning Chai, Benjamin Caine, Vijay Vasudevan, Wei Han, Jiquan Ngiam, Hang Zhao, Aleksei Timofeev, Scott Ettinger, Maxim Krivokon, Amy Gao, Aditya Joshi, Yu Zhang, Jonathon Shlens, Zhifeng Chen, and Dragomir Anguelov. Scalability in perception for autonomous driving: Waymo open dataset. In *Proceedings of the IEEE/CVF Conference on Computer Vision and Pattern Recognition (CVPR)*, June 2020. 5, 18, 30
- [68] Richard S. Sutton. The bitter lesson. <http://www.incompleteideas.net/IncIdeas/BitterLesson.html>, 2019. Accessed: 2024-05-15. 2, 10
- [69] Hugues Thomas, Charles R Qi, Jean-Emmanuel Deschaud, Beatriz Marcotegui, François Goulette, and Leonidas J Guibas. Kpconv: Flexible and deformable convolution for point clouds. In *Proceedings of the IEEE/CVF international conference on computer vision*, pp. 6411–6420, 2019. 3
- [70] Laurens van der Maaten and Geoffrey Hinton. Visualizing data using t-sne. *Journal of Machine Learning Research*, 9(86):2579–2605, 2008. URL <http://jmlr.org/papers/v9/vandermaaten08a.html>. 8
- [71] Ashish Vaswani, Noam Shazeer, Niki Parmar, Jakob Uszkoreit, Llion Jones, Aidan N Gomez, Łukasz Kaiser, and Illia Polosukhin. Attention is all you need. *Advances in neural information processing systems*, 30, 2017. 3
- [72] Tai Wang, Xiaohan Mao, Chenming Zhu, Runsen Xu, Ruiyuan Lyu, Peisen Li, Xiao Chen, Wenwei Zhang, Kai Chen, Tianfan Xue, et al. Embodiedscan: A holistic multi-modal 3d perception suite towards embodied ai. In *Proceedings of the IEEE/CVF Conference on Computer Vision and Pattern Recognition*, pp. 19757–19767, 2024. 1
- [73] Xu Wang, Jiangxia Cao, Zhiyi Fu, Kun Gai, and Guorui Zhou. Home: Hierarchy of multi-gate experts for multi-task learning at kuaishou. In *Proceedings of the 31st ACM SIGKDD Conference on Knowledge Discovery and Data Mining V. 1*, pp. 2638–2647, 2025. 8

- [74] Yue Wang, Yongbin Sun, Ziwei Liu, Sanjay E Sarma, Michael M Bronstein, and Justin M Solomon. Dynamic graph cnn for learning on point clouds. *ACM Transactions on Graphics (tog)*, 38(5):1–12, 2019. 19
- [75] Zhenyu Wang, Ya-Li Li, Hengshuang Zhao, and Shengjin Wang. One for all: Multi-domain joint training for point cloud based 3d object detection. *Advances in Neural Information Processing Systems*, 37:56859–56877, 2024. 1, 2, 3, 4, 5, 6, 22
- [76] Zichen Wang, Ang Cao, Liam J Wang, and Jeong Joon Park. Moe3d: A mixture-of-experts module for 3d reconstruction. *arXiv preprint arXiv:2601.05208*, 2026. 3
- [77] Maximilian Weber, Daniel Wild, Jens Kleesiek, Jan Egger, and Christina Gsaxner. Deep learning-based point cloud registration for augmented reality-guided surgery. In *2024 IEEE International Symposium on Biomedical Imaging (ISBI)*, pp. 1–5. IEEE, 2024. 1
- [78] Tianwen Wei, Bo Zhu, Liang Zhao, Cheng Cheng, Biye Li, Weiwei Lü, Peng Cheng, Jianhao Zhang, Xiaoyu Zhang, Liang Zeng, et al. Skywork-moe: A deep dive into training techniques for mixture-of-experts language models. *arXiv preprint arXiv:2406.06563*, 2024. 7
- [79] Erik Wijmans, Samyak Datta, Oleksandr Maksymets, Abhishek Das, Georgia Gkioxari, Stefan Lee, Irfan Essa, Devi Parikh, and Dhruv Batra. Embodied question answering in photorealistic environments with point cloud perception. In *Proceedings of the IEEE/CVF Conference on Computer Vision and Pattern Recognition*, pp. 6659–6668, 2019. 1
- [80] Xiaoyang Wu, Yixing Lao, Li Jiang, Xihui Liu, and Hengshuang Zhao. Point transformer v2: Grouped vector attention and partition-based pooling. *Advances in Neural Information Processing Systems*, 35:33330–33342, 2022. 3
- [81] Xiaoyang Wu, Li Jiang, Peng-Shuai Wang, Zhijian Liu, Xihui Liu, Yu Qiao, Wanli Ouyang, Tong He, and Hengshuang Zhao. Point transformer v3: Simpler faster stronger. In *Proceedings of the IEEE/CVF conference on computer vision and pattern recognition*, pp. 4840–4851, 2024. 1, 2, 3, 4, 5, 6, 22
- [82] Xiaoyang Wu, Zhuotao Tian, Xin Wen, Bohao Peng, Xihui Liu, Kaicheng Yu, and Hengshuang Zhao. Towards large-scale 3d representation learning with multi-dataset point prompt training. In *Proceedings of the IEEE/CVF Conference on Computer Vision and Pattern Recognition*, pp. 19551–19562, 2024. 1, 2, 3, 4, 5, 6, 8, 22
- [83] Xiaoyang Wu, Daniel DeTone, Duncan Frost, Tianwei Shen, Chris Xie, Nan Yang, Jakob Engel, Richard Newcombe, Hengshuang Zhao, and Julian Straub. Sonata: Self-supervised learning of reliable point representations. In *Proceedings of the Computer Vision and Pattern Recognition Conference*, pp. 22193–22204, 2025. 3
- [84] Yao Wu, Mingwei Xing, Yachao Zhang, Xiaotong Luo, Yuan Xie, and Yanyun Qu. Unidseg: Unified cross-domain 3d semantic segmentation via visual foundation models prior. *Advances in Neural Information Processing Systems*, 37:101223–101249, 2024. 3
- [85] Zhiyu Wu, Xiaokang Chen, Zizheng Pan, Xingchao Liu, Wen Liu, Damai Dai, Huazuo Gao, Yiyang Ma, Chengyue Wu, Bingxuan Wang, et al. Deepseek-vl2: Mixture-of-experts vision-language models for advanced multimodal understanding. *arXiv preprint arXiv:2412.10302*, 2024. 3
- [86] Aoran Xiao, Jiaying Huang, Weihao Xuan, Ruijie Ren, Kangcheng Liu, Dayan Guan, Abdulmoteleb El Saddik, Shijian Lu, and Eric P Xing. 3d semantic segmentation in the wild: Learning generalized models for adverse-condition point clouds. In *Proceedings of the IEEE/CVF conference on computer vision and pattern recognition*, pp. 9382–9392, 2023. 3
- [87] Zhenghuo Xu, Bowen Qu, Yiyang Qi, Sinan Du, Chengjin Xu, Chun Yuan, and Jian Guo. Chartmoe: Mixture of diversely aligned expert connector for chart understanding. *arXiv preprint arXiv:2409.03277*, 2024. 2, 3, 7

- [88] Longyu Yang, Ping Hu, Shangbo Yuan, Lu Zhang, Jun Liu, Hengtao Shen, and Xiaofeng Zhu. Towards explicit geometry-reflectance collaboration for generalized lidar segmentation in adverse weather. In *Proceedings of the Computer Vision and Pattern Recognition Conference*, pp. 139–149, 2025. 3
- [89] Yuanhang Yang, Chaozheng Wang, and Jing Li. Umoe: Unifying attention and ffn with shared experts. *arXiv preprint arXiv:2505.07260*, 2025. 8
- [90] Yanjie Ze, Gu Zhang, Kangning Zhang, Chenyuan Hu, Muhan Wang, and Huazhe Xu. 3d diffusion policy: Generalizable visuomotor policy learning via simple 3d representations. *arXiv preprint arXiv:2403.03954*, 2024. 1
- [91] Biao Zhang and Rico Sennrich. Root mean square layer normalization. *Advances in neural information processing systems*, 32, 2019. 8
- [92] Haimei Zhao, Jing Zhang, Zhuo Chen, Shanshan Zhao, and Dacheng Tao. Unimix: Towards domain adaptive and generalizable lidar semantic segmentation in adverse weather. In *Proceedings of the IEEE/CVF Conference on Computer Vision and Pattern Recognition*, pp. 14781–14791, 2024. 3
- [93] Hengshuang Zhao, Li Jiang, Chi-Wing Fu, and Jiaya Jia. Pointweb: Enhancing local neighborhood features for point cloud processing. In *2019 IEEE/CVF Conference on Computer Vision and Pattern Recognition (CVPR)*, pp. 5560–5568, 2019. doi: 10.1109/CVPR.2019.00571. 3
- [94] Hengshuang Zhao, Li Jiang, Jiaya Jia, Philip HS Torr, and Vladlen Koltun. Point transformer. In *Proceedings of the IEEE/CVF international conference on computer vision*, pp. 16259–16268, 2021. 3
- [95] Jia Zheng, Junfei Zhang, Jing Li, Rui Tang, Shenghua Gao, and Zihan Zhou. Structured3d: A large photo-realistic dataset for structured 3d modeling. In *Proceedings of The European Conference on Computer Vision (ECCV)*, 2020. 5, 6, 18, 19, 21, 30
- [96] Junsheng Zhou, Jinsheng Wang, Baorui Ma, Yu-Shen Liu, Tiejun Huang, and Xinlong Wang. Uni3d: Exploring unified 3d representation at scale. In *International Conference on Learning Representations (ICLR)*, 2024. 3
- [97] Xingyi Zhou, Vladlen Koltun, and Philipp Krähenbühl. Simple multi-dataset detection. In *Proceedings of the IEEE/CVF conference on computer vision and pattern recognition*, pp. 7571–7580, 2022. 1
- [98] Barret Zoph, Irwan Bello, Sameer Kumar, Nan Du, Yanping Huang, Jeff Dean, Noam Shazeer, and William Fedus. St-moe: Designing stable and transferable sparse expert models. *arXiv preprint arXiv:2202.08906*, 2022. 3

## APPENDIX

For a thorough understanding of our Point-MoE, we have compiled a detailed Appendix. The table of contents below offers a quick overview and will guide to specific sections of interest.

## CONTENTS

<b>A</b>	<b>Limitations, Licenses and Risks</b>	<b>18</b>
A.1	Limitations . . . . .	18
A.2	Artifacts and License . . . . .	18
A.3	Ethical concerns and Risks . . . . .	18
<b>B</b>	<b>Additional Experiments</b>	<b>19</b>
B.1	Experiment Datasets . . . . .	19
B.2	Additional Results and Analysis . . . . .	19
B.3	Additional Main Results . . . . .	21
<b>C</b>	<b>Additional Visualization and Discussions on Point-MoE</b>	<b>22</b>
C.1	Semantic Concept Distribution over Experts . . . . .	22
C.2	Expert Evolution. . . . .	29
C.3	More Expert Choice Visualization . . . . .	30

## A LIMITATIONS, LICENSES AND RISKS

## A.1 LIMITATIONS

Within our compute budget, we present a comprehensive study of MoE for point clouds—covering placement, expansion, routing choices (top- $k$ , capacity factor, load balancing), and mixed-domain batching—with consistent gains. However, compute remains the primary bottleneck, capping Point-MoE’s scale (experts, width, depth), training schedule, and number of jointly trained datasets. We therefore leave systematic scaling (e.g., expert count/width, per-stage sharing, alternative routers) to future work. Finally, because 3D semantic segmentation depends on costly human labels, we plan to pursue self-supervised pretraining on diverse unlabeled point clouds to reduce annotation effort and improve generalization. We hope these results serve as a simple, strong baseline and a useful reference point for future works.

## A.2 ARTIFACTS AND LICENSE

We report a list of licenses for all datasets and code used in our experiment in Tab. 6. We strictly follow all the datasets and code licenses and limit the scope of these datasets and code to academic research only.

## A.3 ETHICAL CONCERNS AND RISKS

This study does *not* involve human subjects or annotators. All experiments are performed on publicly released 3D benchmarks—ScanNet [19], Structured3D [95], S3DIS [1], Matterport3D [10], SemanticKITTI [5], nuScenes [9], and Waymo [67]—each distributed under their respective licences. Although these datasets are widely used, they may still reflect geographic, socioeconomic, or sensor-specific biases, which Point-MoE could inherit or amplify when deployed in real-world applications. We therefore encourage future work to develop debiasing techniques, to curate more balanced point-cloud corpora, and to incorporate fairness-oriented evaluation metrics so that cross-domain 3D models can serve all communities responsibly.

Table 6: License information for the scientific artifacts used.

Data Sources	URL	License
ScanNet [19]	<a href="#">Link</a>	ScanNet Terms of Use
Structured3D [95]	<a href="#">Link</a>	Structured3D Terms of Use
S3DIS [1]	<a href="#">Link</a>	CC BY-NC 4.0
Matterport3D [10]	<a href="#">Link</a>	Matterport3D License
nuScenes [9]	<a href="#">Link</a>	CC BY-NC-SA 4.0
SemanticKITTI [5]	<a href="#">Link</a>	CC BY-NC-SA 3.0
Waymo Open Dataset [74]	<a href="#">Link</a>	Waymo Research License
Software Code	URL	License
Pointcept [18]	<a href="#">Link</a>	MIT License

Table 7: Overview of 3D Semantic Segmentation datasets differences. L, W, and H represent the length, width, and height. For all datasets, we use the raw point clouds to obtain the point ranges.

Dataset	Sensor	Point Range (m)	Scene Type
ScanNet [19]	Reconstructed	L=[-2.13, 17.12], W=[-1.46, 18.19], H=[-0.38, 6.97]	indoor
S3DIS [1]	Reconstructed	L=[-37.93, 29.93], W=[-26.08, 46.06], H=[-2.65, 6.58]	indoor
Structured3D [95]	Synthetic	L=[-53.70, 52.05], W=[-82.07, 53.43], H=[-0.78, 15.49]	indoor
Matterport3D [10]	RGB-D Camera	L=[-34.99, 72.17], W=[-57.85, 75.65], H=[-6.79, 10.21]	indoor
SemanticKITTI [5]	64-beam LiDAR	L=[-81.15, 80.00], W=[-80.00, 79.99], H=[-32.49, 3.51]	outdoor
Waymo [74]	64-beam LiDAR	L=[-74.98, 76.53], W=[-75.00, 75.00], H=[-18.36, 6.78]	outdoor
nuScenes [9]	32-beam LiDAR	L=[-105.17, 105.25], W=[-105.30, 105.17], H=[-53.42, 20.01]	outdoor

## B ADDITIONAL EXPERIMENTS

### B.1 EXPERIMENT DATASETS

We compare a diverse set of 3D semantic segmentation datasets spanning both indoor and outdoor environments. ScanNet [19] is a large-scale indoor RGB-D dataset reconstructed from real-world scans of apartments and offices. S3DIS [1] contains real indoor scans of commercial buildings, providing richly annotated scenes with diverse architectural structures. Structured3D [95] is a synthetic dataset based on photo-realistic rendered scenes from CAD models, offering clean labels and dense annotations. Matterport3D [10] consists of real RGB-D scans captured in a wide range of residential environments, covering multiple floors and room types.

For outdoor settings, SemanticKITTI [5] provides point clouds captured by a 64-beam LiDAR mounted on a car, annotated for semantic understanding of dynamic street scenes. Waymo Open Dataset [74] extends this setup with more diverse driving environments and higher annotation quality, collected using a custom autonomous vehicle sensor suite. nuScenes [9] offers multimodal driving data, including LiDAR scans, captured in urban environments with complex traffic scenarios and longer temporal contexts. We include detailed dataset statistic in Tab. 7.

Furthermore, we provide detailed per-class comparisons on semantic classes for both indoor and outdoor datasets, as shown in Fig. 8 and Fig. 9.

### B.2 ADDITIONAL RESULTS AND ANALYSIS

**Domain Detector.** To enable domain-aware models at inference time—where ground-truth dataset labels are unavailable—we train a lightweight classifier to predict the domain of an input point cloud. This domain detector serves a purely functional role: it allows domain-conditioned variants of Point-MoE and other baselines to operate in realistic deployment scenarios where users may supply point clouds from unknown or mixed sources. During training, we observe that strong data augmentations (*e.g.*, grid dropout or random cropping) reduce the classifier’s reliability by masking domain-specific cues. To preserve dataset-level characteristics critical for this task, we disable most augmentations and apply only minimal point cropping for efficiency. The domain detector converges quickly, with accuracy stabilizing after just a few epochs. As shown in Fig. 5, it achieves high



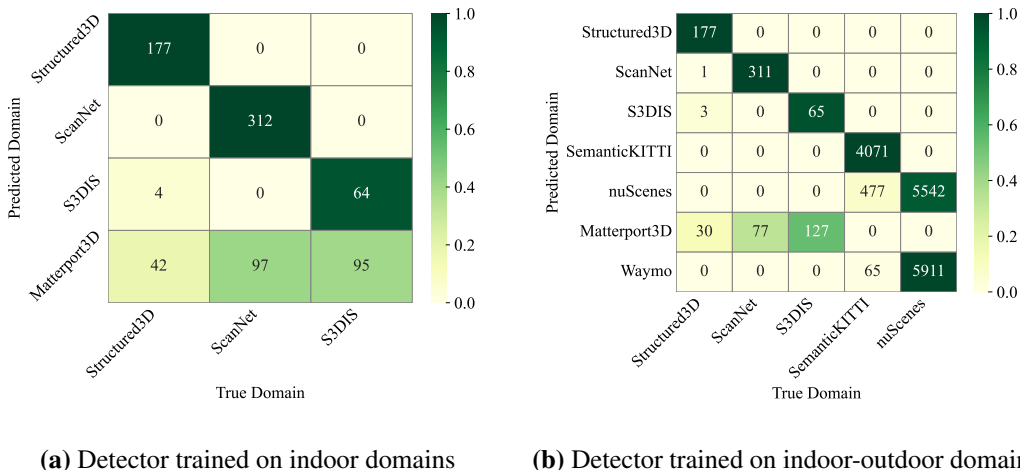


Figure 5: **Domain Classification Confusion Matrices.** (a) Confusion matrix for a domain detector trained only on indoor datasets: Structured3D [95], ScanNet [19], and S3DIS [1]. (b) Confusion matrix for a detector trained on both indoor and outdoor datasets: Structured3D [95], ScanNet [19], S3DIS [1], SemanticKITTI [5], and nuScenes [9]. In both cases, we evaluate generalization to unseen domains. Values are normalized per predicted domain (row-wise).

Table 11: **MoE on a sparse convolutional backbone (OA-CNN).** Numbers are mIoU. Rows (1)–(4) use the public OA-CNN implementation (with a language-guided head for cross-dataset evaluation). (1)–(3) train on a single dataset; (4) joint-trains on ScanNet, Structured3D, and S3DIS; (5) replace SparseCNN with MoE-CNN using top-2 routing.

Model	ScanNet	Structured3D	S3DIS	Matterport3D	Average
(1) OA-CNN-S3DIS	5.70	3.8	65.3	5.4	20.6
(2) OA-CNN-ScanNet	72.6	21.6	8.4	37.4	35.0
(3) OA-CNN-Structured3D	20.8	65.6	6.8	18.9	28.0
(4) OA-CNN	71.6	59.0	60.6	37.8	57.3
(5) OA-CNN-MoE	<b>72.0</b>	<b>65.3</b>	<b>63.0</b>	<b>40.2</b>	<b>60.1</b>

### B.3 ADDITIONAL MAIN RESULTS

**Results without precise evaluator.** The results reported in Tab. 1 are obtained using the precise evaluator provided by Pointcept [18]. The precise evaluator first splits each scene into multiple overlapping chunks, then performs model inference on each chunk individually. After inference, it aggregates predictions across chunks through a voting mechanism to refine the final output. We typically observe a gain of 2–4% in accuracy on each dataset using this method. While effective, the precise evaluator introduces additional runtime overhead during evaluation. Moreover, we note that this form of ensembling may hurt overall performance when the model’s predictions are unreliable in early chunks, as incorrect outputs are also accumulated in the final vote. To support convenient and reproducible benchmarking for the community, we include results with the precise evaluator in the main text and provide additional baseline results without it elsewhere in the paper.

From both Tab. 12 and Tab. 13, we observe that Point-MoE outperforms the baselines in most domains in both the indoor-only and indoor-outdoor joint training settings. These results are consistent with those obtained using the precise evaluator reported in the main text. We do not observe any contradictory trends, as the precise evaluator typically improves all methods by a similar margin of 2–4%. As such, our analysis and conclusions align closely with those presented in the main text. To ensure a strong baseline, we add mixed-dataset training and tune hyper-parameters, reporting the baseline with its best configuration. To be specifically, we apply mix-dataset training for baselines

Table 12: **Main Results without Precise Evaluator.** Each model is trained jointly on three indoor datasets and evaluated without precise evaluator. \* indicates that each training batch combines samples from multiple datasets, methods with \*\* use mix dataset batch and layernorm [3].

Methods	Params	Activated	ScanNet	Structured3D	S3DIS	Matterport3D	Average
			Val	Val	Area5	Val	
<i>Single-dataset Training</i>							
PTv3-ScanNet [81]	46M	46M	74.4	19.4	8.5	37.9	35.1
PTv3-Structured3D [81]	46M	46M	20.0	78.0	7.0	19.5	31.1
PTv3-S3DIS [81]	46M	46M	4.9	3.4	66.1	5.2	19.9
PTv3-Matterport3D [81]	46M	46M	52.7	23.0	9.5	53.6	34.7
<i>Multi-dataset Joint Training</i>							
PTv3-S [81]	46M	46M	48.4	57.8	44.1	27.8	44.5
PTv3-S* [81] [81]	46M	46M	67.7	45.9	62.5	34.9	52.8
PTv3-S** [81]	46M	46M	70.0	56.0	66.9	35.6	57.1
PTv3-L [81]	97M	97M	57.1	58.1	40.3	31.0	46.6
PTv3-L* [81]	97M	97M	73.3	57.5	67.2	38.4	59.1
PTv3-L** [81] [81]	97M	97M	74.0	67.4	67.8	40.6	62.5
PPT-S [75, 82]	47M	47M	74.2	58.2	61.0	24.3	54.4
PPT-L [75, 82]	98M	98M	74.7	64.9	62.0	27.8	57.4
Point-MoE-S	59M	52M	74.5	66.9	<b>68.6</b>	40.1	62.5
Point-MoE-L	100M	60M	<b>75.1</b>	<b>69.3</b>	68.5	<b>41.3</b>	<b>63.6</b>

Table 13: **Main Results on Indoor and Outdoor Scenes without Precise Evaluator.** Models are trained jointly on both indoor and outdoor datasets.\* indicates that each training batch combines samples from multiple datasets, methods with \*\* use mix dataset batch and layernorm [3].

Methods	Params	Activated	ScanNet	Structured3D	S3DIS	nuScenes	SemKITTI	Matterport3D	Waymo	Average
			Val	Val	Area5	Val	Val	Val	Val	
PTv3-L [81]	97M	97M	55.9	47.6	19.3	42.9	35.3	31.8	12.4	35.0
PTv3-L* [81]	97M	97M	73.4	61.9	61.4	64.7	59.3	38.9	22.8	54.6
PTv3-L** [81]	97M	97M	73.6	61.3	65.1	64.5	59.7	37.1	21.9	54.7
PPT-L [75, 82]	98M	98M	75.2	67.5	61.0	57.2	<b>64.0</b>	20.8	16.0	51.7
Point-MoE-L	100M	60M	<b>76.2</b>	<b>70.1</b>	<b>67.9</b>	<b>68.9</b>	63.3	<b>40.7</b>	<b>23.4</b>	<b>58.6</b>

we can directly apply without code modification and we also find layernorm is empirically better for the baselines.

## C ADDITIONAL VISUALIZATION AND DISCUSSIONS ON POINT-MOE

### C.1 SEMANTIC CONCEPT DISTRIBUTION OVER EXPERTS

**Expert Specialization Word Cloud.** To visualize expert specialization, we collect the semantic predictions from each expert in the decoder layers of Point-MoE. During inference, we log which expert is selected for each point and record the corresponding semantic prediction. For each expert, we compute the frequency distribution of predicted classes across the entire validation set and display the most frequent class as a word cloud. Colors indicate the originating dataset of the prediction (*e.g.*, ScanNet, S3DIS, etc.), providing insight into cross-domain consistency.

We observe several interesting patterns in the expert specialization behavior. (1) In each decoder layer, there is typically at least one expert with a strong preference for outdoor data. For example, Decoder 0\_0 Expert 7, Decoder 1\_1 Expert 1, and Decoder 2\_1 Expert 2 predominantly handle outdoor scenes. (2) Generic or ambiguous semantic classes such as *otherfurniture* or *other-ground* never dominate the assignment of any expert, suggesting that these classes are more diffusely distributed and do not concentrate through the routing mechanism.

From the visualization in Fig. 6, we observe several notable trends. Specialization emerges clearly: within each decoder block, experts tend to focus on semantically coherent regions such as *bed*, *bathub*, *window*, or *trailer*, suggesting that experts develop functional roles under shared supervision. In many blocks, multiple experts cover similar classes, yet differ in dataset association, indicating potential

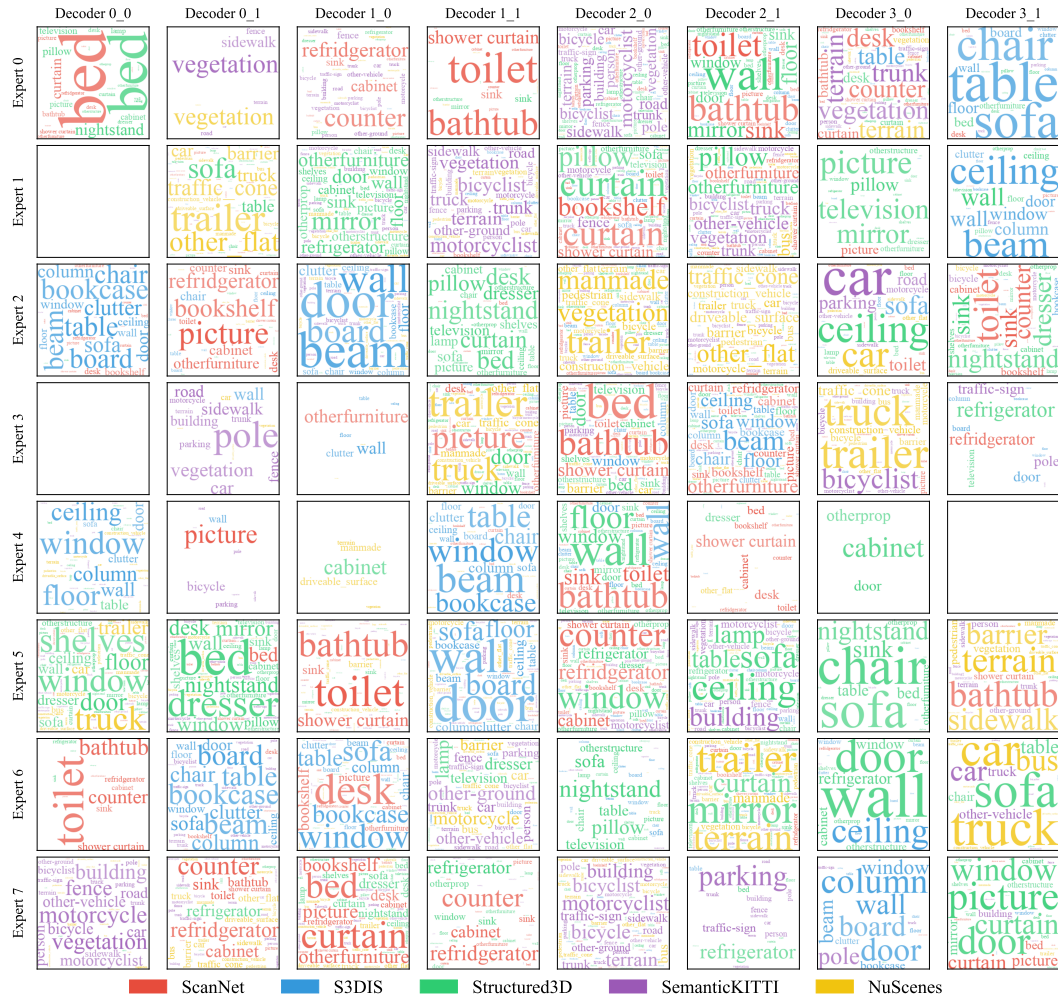


Figure 6: **Expert Specialization Word Cloud.** All classes’ frequencies of selecting their top-1 expert are measured on the validation set. Colors indicate the originating dataset of the class (e.g., ScanNet, S3DIS, etc.), providing insight into cross-domain consistency.

cross-domain generalization. For instance, certain experts across blocks frequently predict *bed* or *toilet* across multiple indoor datasets, hinting at robust feature preferences. We also observe signs of dataset sensitivity. Classes like *trailer*, *parking*, and *terrain* appear predominantly in SemanticKITTI and nuScenes, while *sink*, *shower curtain*, and *dresser* are more common in Structured3D. Comparing across decoder layers, earlier blocks display a broader mix of classes per expert, while deeper blocks exhibit more focused and object-specific specialization, reflecting an increasing semantic refinement through the decoding process.

These findings suggest that Point-MoE encourages structured representation learning, where each expert in a given layer implicitly captures recurring semantic or geometric patterns, even without explicit specialization objectives or layer-to-layer consistency.

**Expert Probability Stack Visualization.** To complement the word cloud analysis, we provide fine-grained views of expert behavior in Fig. 7, Fig. 8, Fig. 9 and Fig. 10. For each semantic class, we visualize the soft routing probabilities across all experts within a specific decoder block. Each horizontal bar corresponds to a class, segmented proportionally by the probability of top-1 expert assignment to each expert. This representation allows us to examine how responsibilities are distributed across experts for different categories.

We observe that certain semantic classes are strongly associated with a small number of experts. For example, *bed*, *bathub*, and *toilet* are consistently routed to a narrow subset of experts, reflecting high specialization. In contrast, classes such as *wall* and *vegetation* are distributed across multiple experts, likely due to their spatial extent and ubiquity in scenes. Some experts show broad activation across diverse classes, while others are more selective, indicating a balance between general-purpose and task-specific routing. Several consistent patterns emerge in the decoder. In Decoder Layer 3 Block 0, both *truck* and *trailer* are primarily assigned to Expert 3, suggesting structural similarity. In Decoder Layer 3 Block 1, *dresser*, *nightstand*, and *counter* are all routed to Expert 2, reflecting shared visual or functional features. In Decoder Layer 0 Block 1, *traffic cone* and *barrier* exhibit nearly identical routing distributions, likely due to their geometric similarity and outdoor context. These observations confirm that the model learns structured yet flexible routing strategies, shaped by both semantic identity and spatial context.

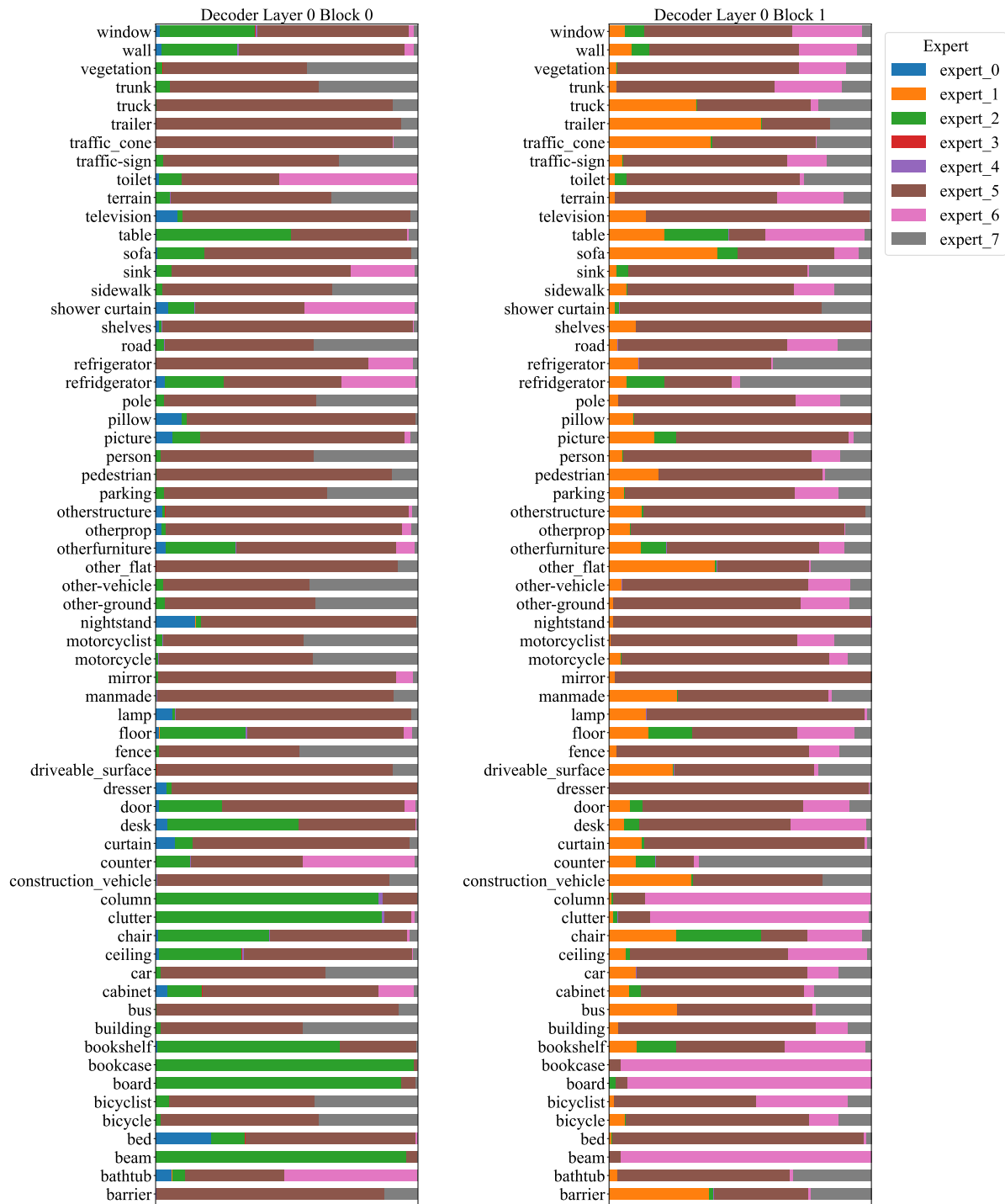


Figure 7: Expert Choices Visualization for Decoder Layer 0.

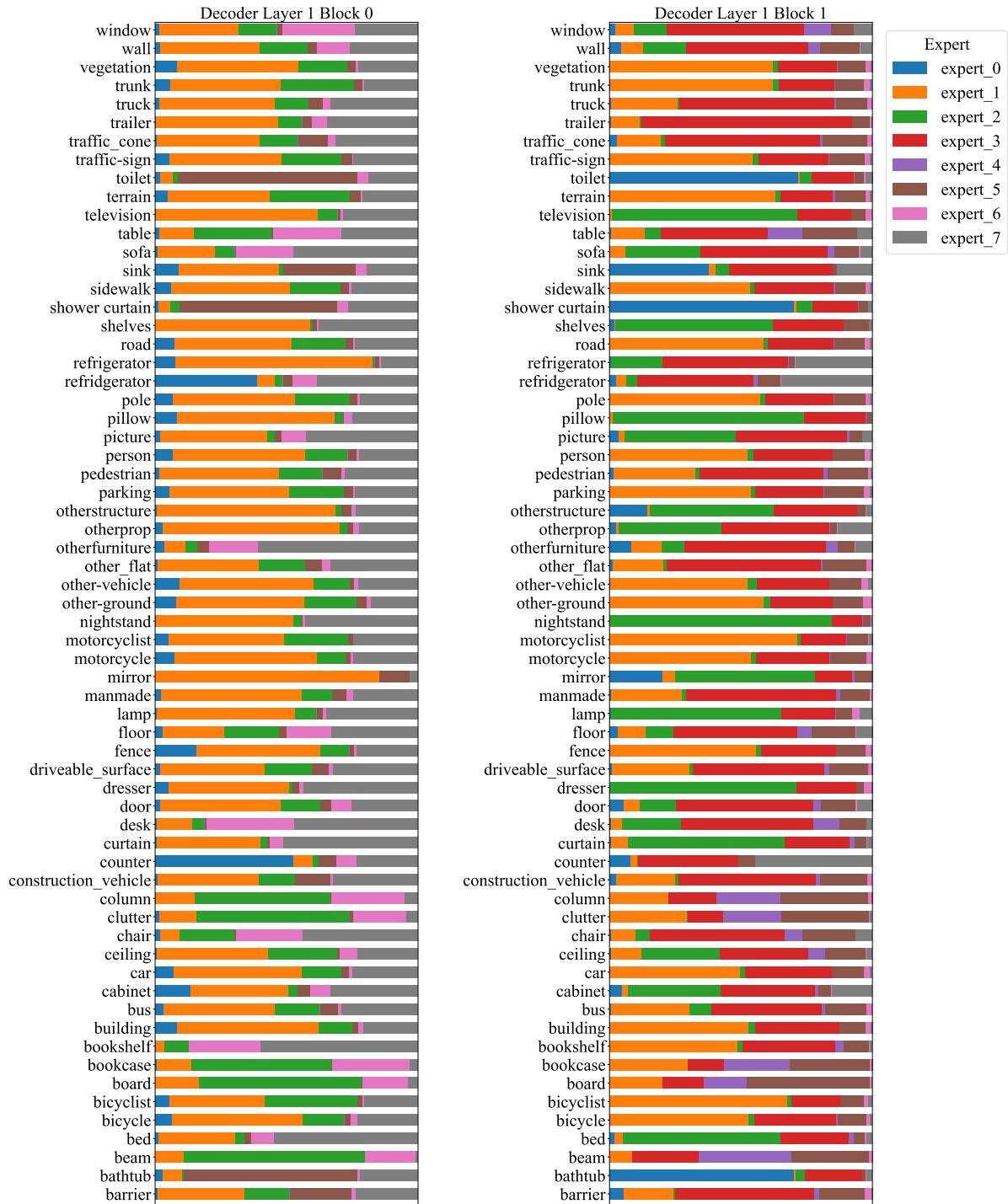


Figure 8: Expert Choices Visualization for Decoder Layer 1.

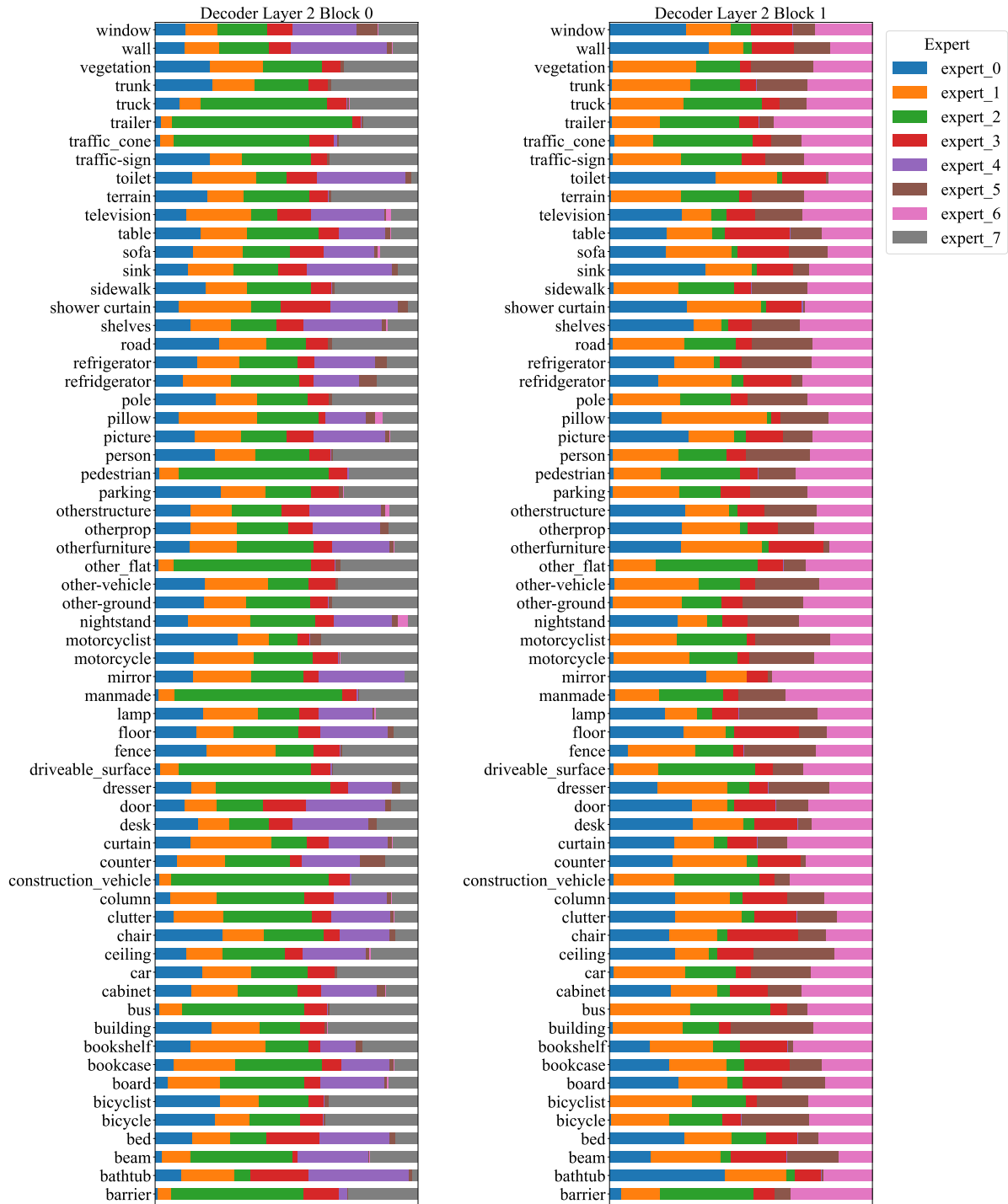


Figure 9: Expert Choices Visualization for Decoder Layer 2.

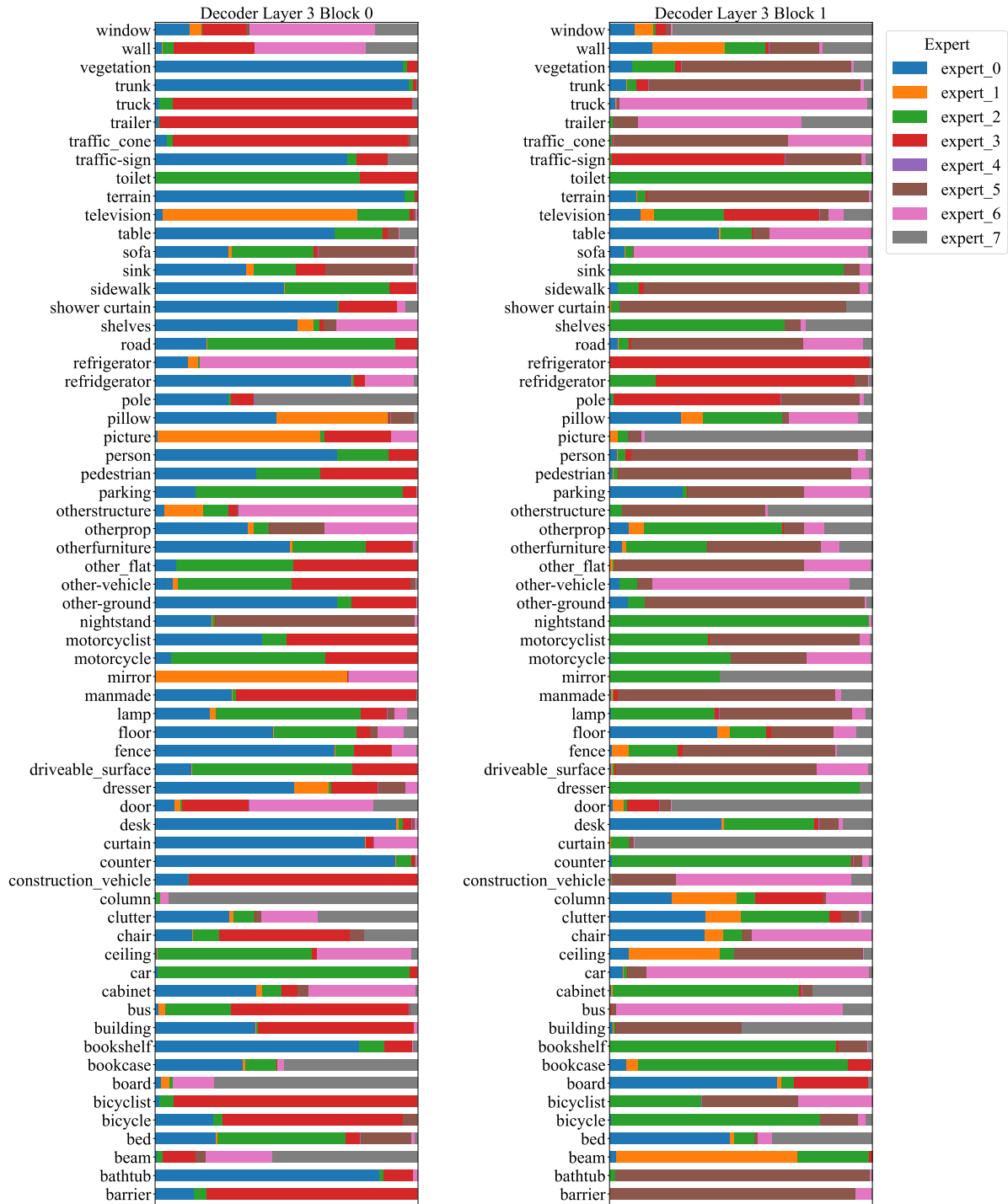


Figure 10: Expert Choices Visualization for Decoder Layer 3.

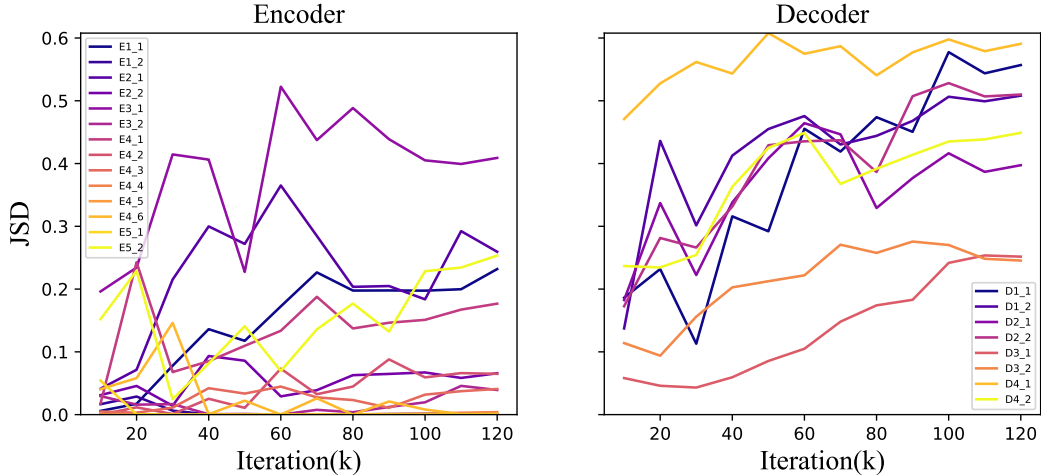


Figure 11: **JSD Dynamics During Training.** We visualize the Jensen-Shannon Divergence (JSD) between expert assignment distributions across datasets to study how expert specialization emerges over time. The plots illustrate JSD dynamics across training iterations for both encoder and decoder layers.

## C.2 EXPERT EVOLUTION.

In Fig. 11, we track the *Jensen-Shannon Divergence (JSD)* between expert assignment distributions across different datasets every 10k training iterations to analyze how expert specialization evolves over time. Let  $P_1, P_2, \dots, P_n$  denote the expert routing distributions for each of the  $n$  datasets, where each  $P_i$  is a categorical distribution over experts. Specifically, let  $P_i(e)$  denote the fraction of tokens from dataset  $i$  that are routed to expert  $e$ . Let  $\pi_1, \pi_2, \dots, \pi_n$  be the corresponding weights assigned to each dataset, satisfying  $\sum_{i=1}^n \pi_i = 1$ . These weights reflect the proportion of tokens contributed by each dataset. The Jensen-Shannon Divergence is defined as:

$$\text{JSD}_\pi(P_1, P_2, \dots, P_n) = H\left(\sum_{i=1}^n \pi_i P_i\right) - \sum_{i=1}^n \pi_i H(P_i),$$

where  $H(P) = -\sum_x P(x) \log P(x)$  denotes the Shannon entropy. This formulation captures the degree of divergence between datasets in terms of how they utilize the experts, providing a measure of specialization and separation over time.

In the early stages (10k–30k), JSD values remain low across most experts, indicating that the routing behavior is largely uniform across datasets and experts have not yet developed distinct roles. Between 40k and 60k iterations, we begin to observe divergence among certain experts, marking the onset of specialization. This trend continues and becomes more pronounced by 80k iterations, where several experts display increasingly distinct assignment distributions. By 100k iterations, the JSD curves stabilize, suggesting that expert roles have converged. Some experts diverge earlier and more sharply, indicating faster specialization, while others evolve more gradually. Overall, this analysis confirms that expert diversity in Point-MoE is not predefined but emerges progressively through training.

In the encoder, we observe that some experts maintain JSD values close to zero throughout training, suggesting that their routing behavior remains largely random and undifferentiated. This observation aligns with Fig. 4, where certain encoder experts do not exhibit clear dataset- or task-specific specialization. This raises the possibility that not all encoder layers require MoE modules, or that additional regularization or training signals may be needed to encourage expert differentiation in the encoder. Nonetheless, we do observe that some encoder experts do specialize over time, indicating that meaningful expert roles can still emerge under the right conditions.

In the decoder, we observe that all experts exhibit high JSD values, indicating that their routing behavior becomes highly specialized and dataset-dependent. Additional visualizations of expert assignments can be found in Sec. C.3, further illustrating this specialization.

### C.3 MORE EXPERT CHOICE VISUALIZATION

Fig. 12, Fig. 13, Fig. 14, Fig. 15, Fig. 16, Fig. 17, and Fig. 18 showcase expert assignments for a validation scene across all layers. Due to the hierarchical structure of the PTV3 backbone, we observe denser point cloud representations at the input and output stages, with sparser intermediate features. This design leads to visibly varying point densities and detail levels across the network. We also observe block-like artifacts in some visualizations, which are likely attributed to PTV3’s point serialization strategy. In the encoder, certain experts occasionally exhibit collapsed or spatially clustered behavior—a phenomenon we refer to as “expert clasping.” A deeper investigation into this behavior is left for future work. In the decoder layers, expert assignments closely resemble semantic segmentation outputs, even though the visualizations reflect only expert routing decisions rather than predicted labels. This suggests that experts naturally specialize in semantically coherent regions, despite the absence of explicit supervision guiding their roles.

In Fig. 12, we observe that early encoder layers primarily rely on geometric cues for expert routing. For example, certain experts—such as the green one—are consistently activated along object boundaries, including the edges of desks and chairs, while others tend to dominate on flat or horizontal surfaces. In the decoder layers, expert assignments become more semantically meaningful, with different experts focusing on specific object categories such as desks, chairs, walls, and floors.

In Fig. 13, we observe a similar overall pattern to ScanNet [19]. In the encoder, expert assignments are primarily driven by local geometric structure, with clear attention to furniture boundaries and wall intersections. Notably, edge-aware routing persists deeper into the encoder—for example, in encoder layer 2 block 0, certain experts remain focused on object contours. In the decoder, expert activation becomes increasingly aligned with semantic regions, such as tables, chairs, and structural elements. Despite the architectural and layout differences from ScanNet, the expert routing in S3DIS remains semantically consistent across the scene.

Fig. 14 illustrates expert routing on Structured3D [95], a synthetic dataset. Compared to real-world datasets, the expert assignment patterns appear sharper and more consistent, likely due to the absence of sensor noise and reconstruction artifacts. Some experts are clearly focused on flat regions, such as beds or floor. In the decoder layers, expert specialization aligns closely with object instances, and the separation across semantic regions is more distinct and well-defined, highlighting the benefits of clean, synthetic geometry for expert differentiation.

Fig. 15 presents expert routing on Matterport3D [10], which contains complex residential environments. In the early encoder layers, we observe clear expert usage patterns—for instance, a distinct separation between vertical and horizontal surfaces. In the decoder layers, expert assignments become more semantically meaningful, with experts specializing in large structural elements such as floors and ceilings, as well as common household objects like counters, sofas, and chairs. Notably, Matterport3D is *not* included in the training set, so this behavior reflects Point-MoE’s ability to generalize expert specialization to *unseen* domains.

In Fig. 16, we examine an outdoor scene from SemanticKITTI [5], characterized by sparse LiDAR data. Despite the limited geometric density, the model still exhibits meaningful expert routing: nearby points tend to be assigned to certain experts, while distant points activate others. Although the transition from geometry-driven to semantically informed expert assignment remains observable, it appears noisier due to the inherent sparsity and irregularity of the input point cloud.

Fig. 17 shows expert routing on nuScenes [9], an outdoor dataset with lower-resolution LiDAR data. In the encoder layers, expert assignments appear more fragmented, likely due to the reduced point density. Nonetheless, we observe that closer points are often routed to specific experts, while distant points are handled by others, indicating a spatially aware routing pattern. In the decoder layers, expert assignments become more semantically coherent, with specialization emerging for vehicle bodies, building facades, and road surfaces based on point position and distance.

Fig. 18 presents expert routing on Waymo [67], an unseen dataset characterized by 64-beam LiDAR scans. In the encoder, experts exhibit structured activation patterns even in early layers, with clear delineation between flat surfaces and protruding objects. In the decoder layers, expert routing becomes more semantically aligned, with experts consistently activated over road surfaces, vehicle bodies, and trees. The assigned regions remain compact and well-separated.

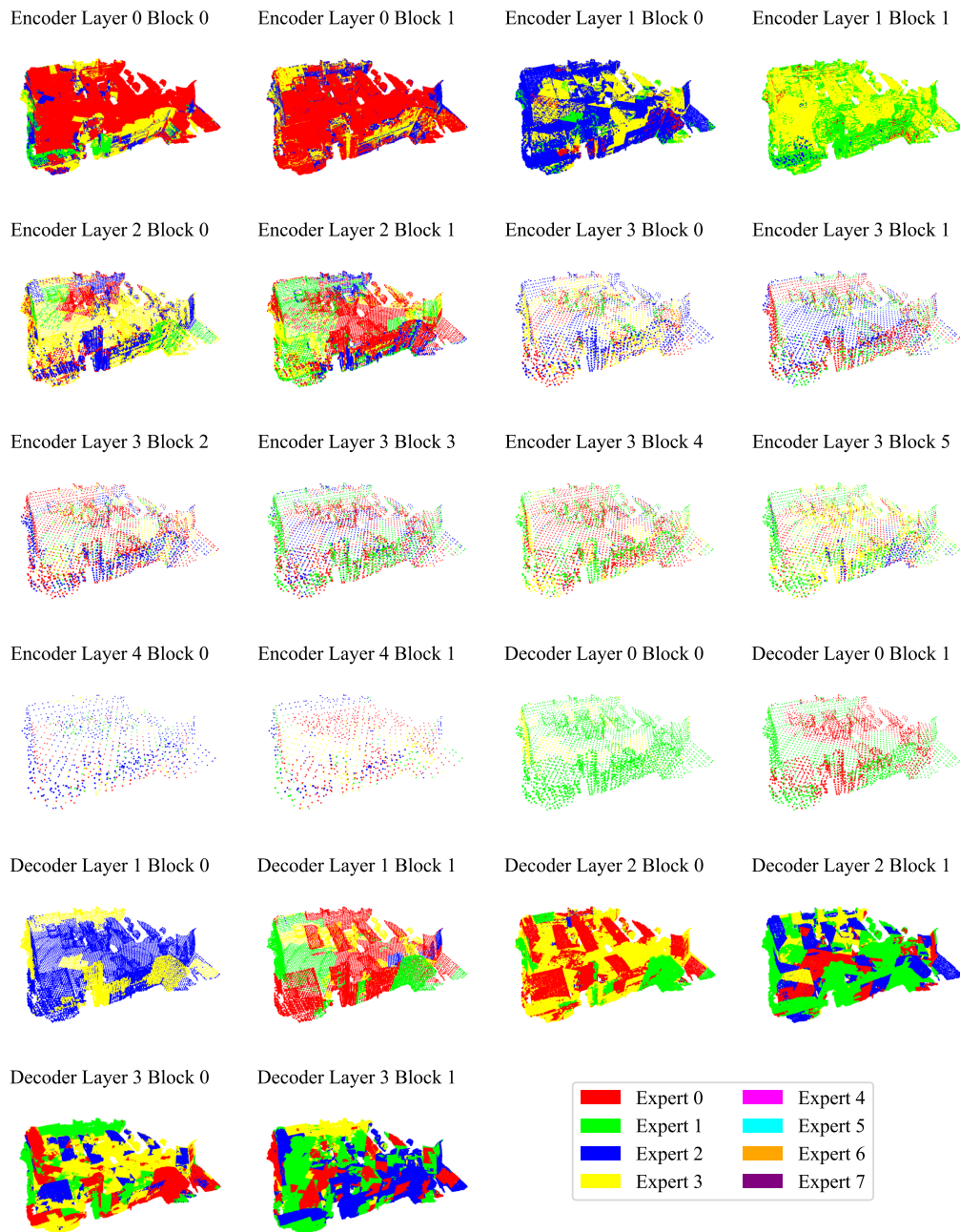


Figure 12: **Point-MoE’s Expert Choice Visualization on ScanNet.** Each point is colored by its assigned expert across encoder and decoder blocks. Early layers show structured expert usage, while deeper layers exhibit more mixed routing, reflecting the evolving representation dynamics throughout the network.

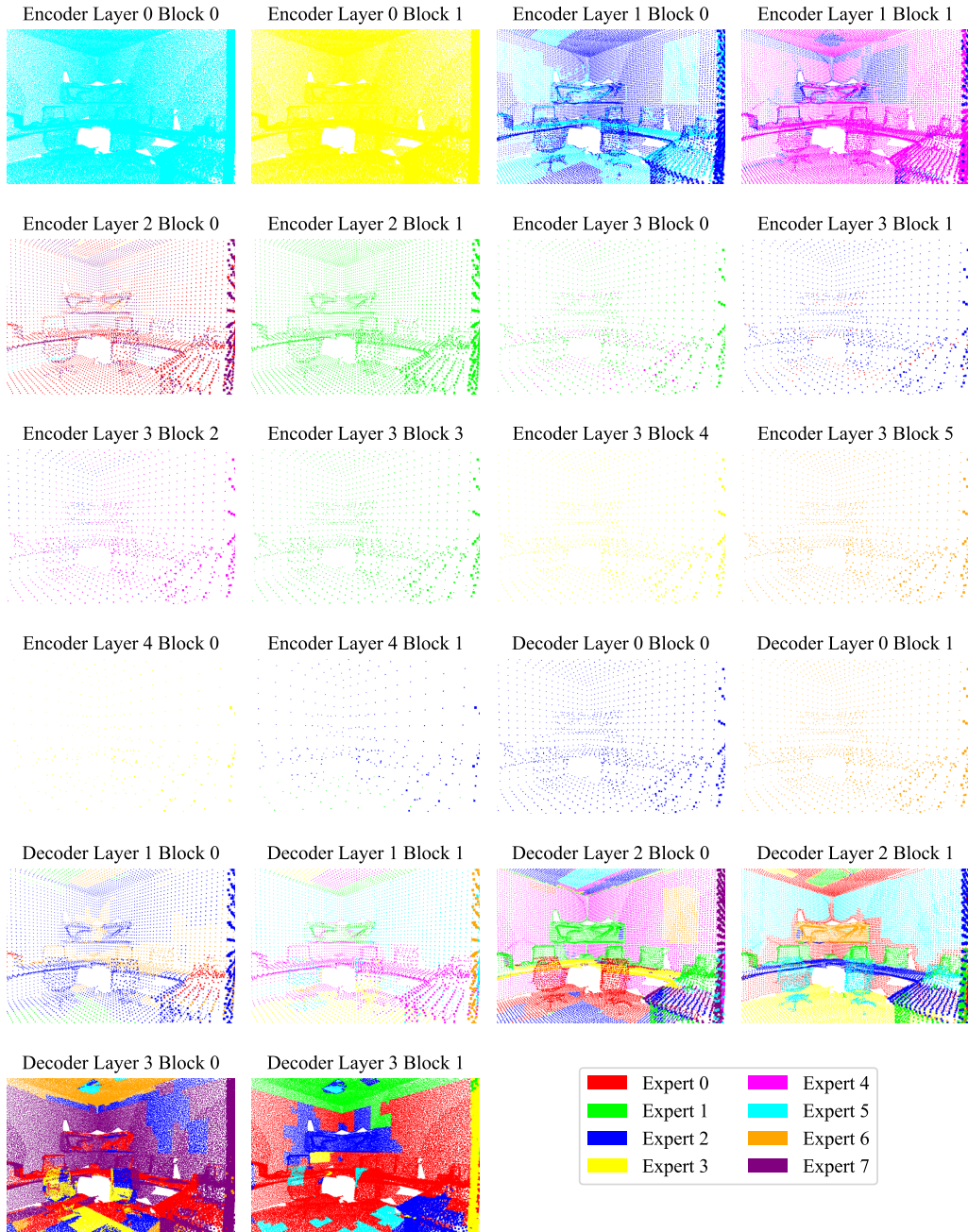


Figure 13: **Point-MoE’s Expert Choice Visualization on S3DIS.** Each point is color-coded based on the expert it was routed to across both encoder and decoder blocks. The earlier layers demonstrate clear structure in expert assignments, whereas the later layers reveal more diverse routing patterns, indicating evolving feature representations.

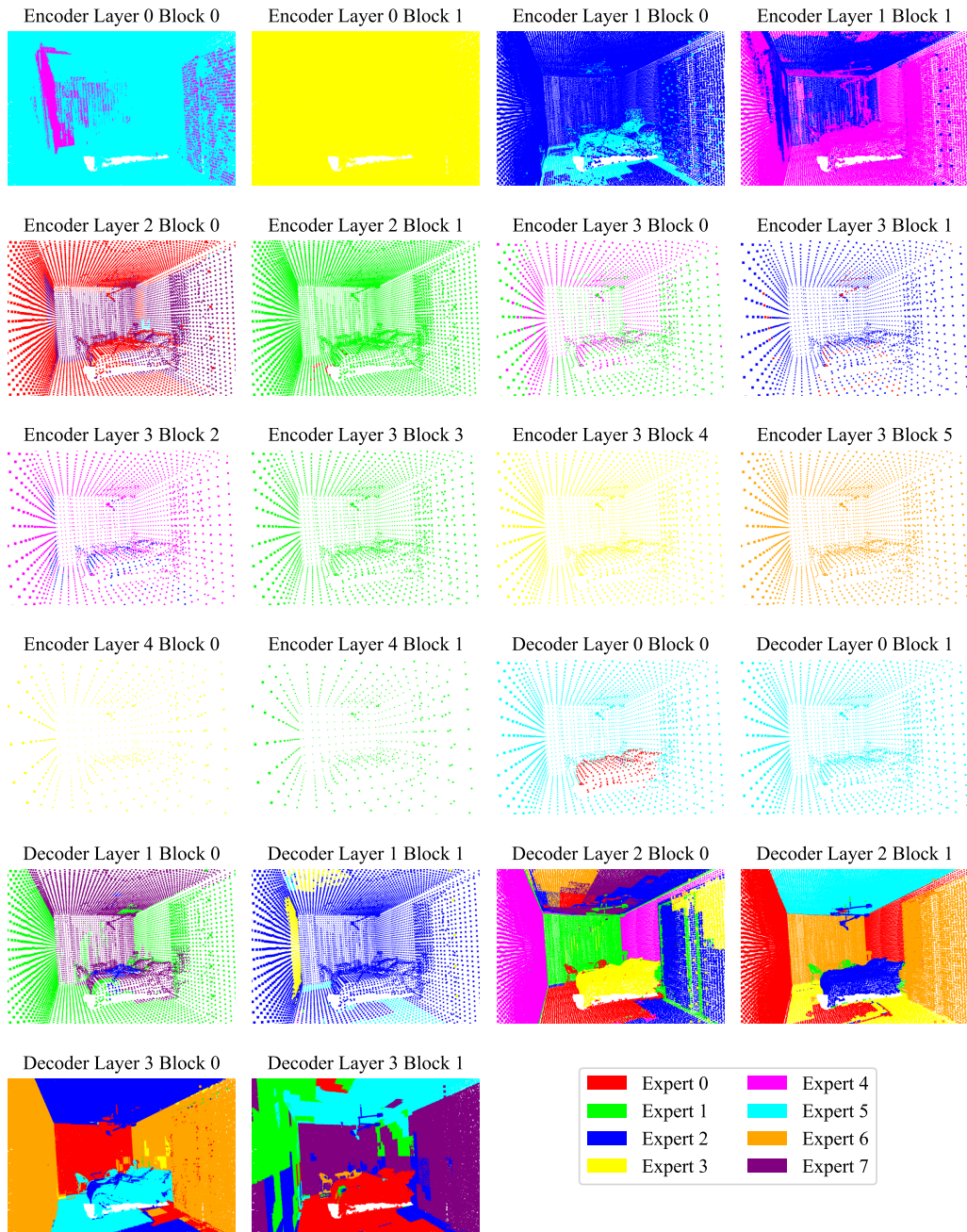


Figure 14: **Point-MoE’s Expert Choice Visualization on Structured3D.** Points are colored by their designated experts in the encoder and decoder. While the initial layers display consistent expert allocation, the deeper layers show a blend of routing decisions, highlighting the network’s shifting representational strategy.



Figure 15: **Point-MoE’s Expert Choice Visualization on Matterport3D.** Color represents the expert assigned to each point throughout the encoder and decoder. Structured expert usage is visible in early stages, transitioning to more varied routing in deeper layers, signaling changes in how features are processed.

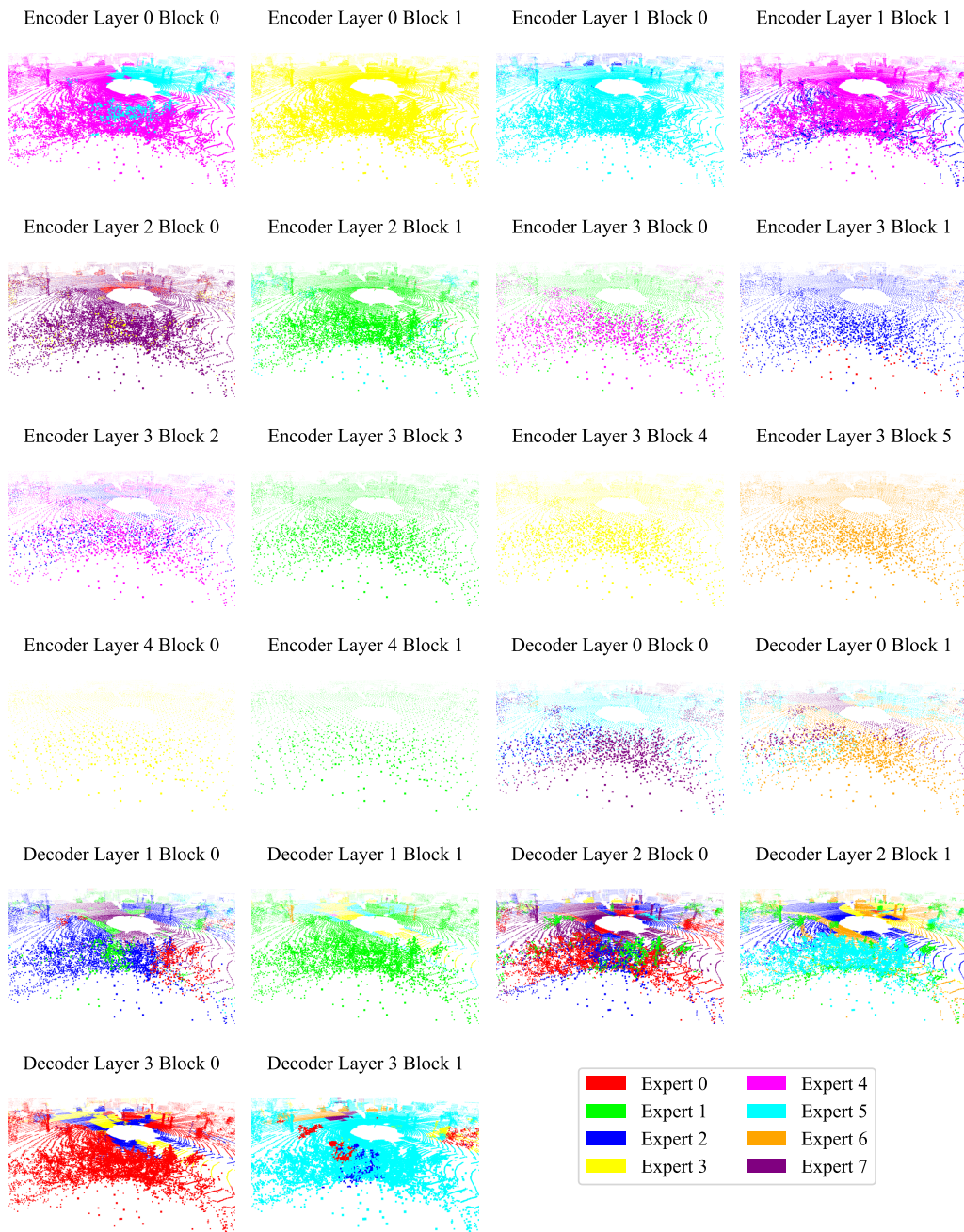


Figure 16: **Point-MoE’s Expert Choice Visualization on SemanticKITTI.** The expert responsible for each point, shown through color, spans the encoder and decoder blocks. Initially, expert usage is highly organized, but becomes more dispersed in later layers, capturing the transformation in representation over depth.

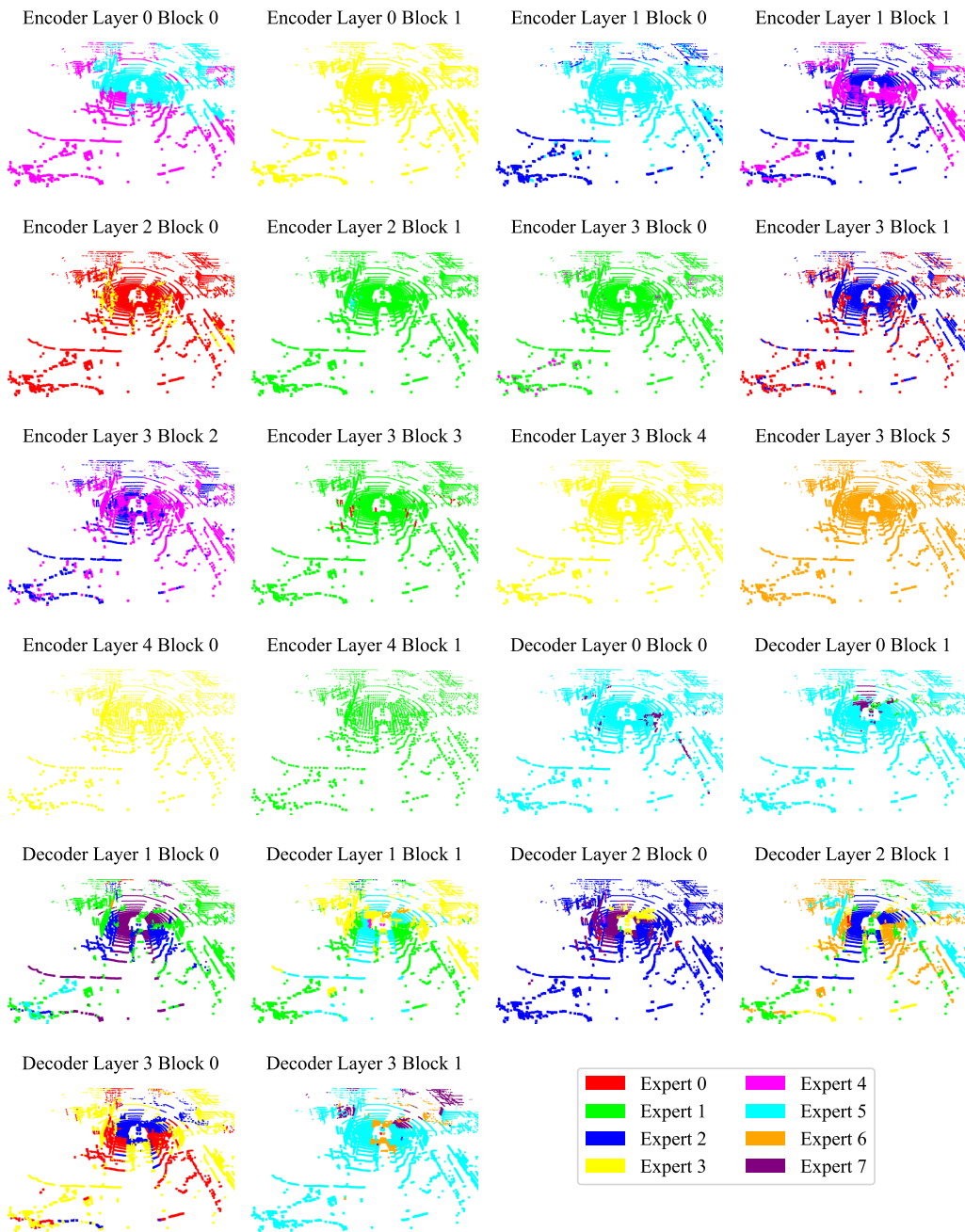


Figure 17: **Point-MoE’s Expert Choice Visualization on NuScene.** Each point is colored according to its corresponding expert across the network’s layers. Early encoder and decoder blocks exhibit distinct expert patterns, while deeper layers demonstrate a more distributed and dynamic routing behavior.

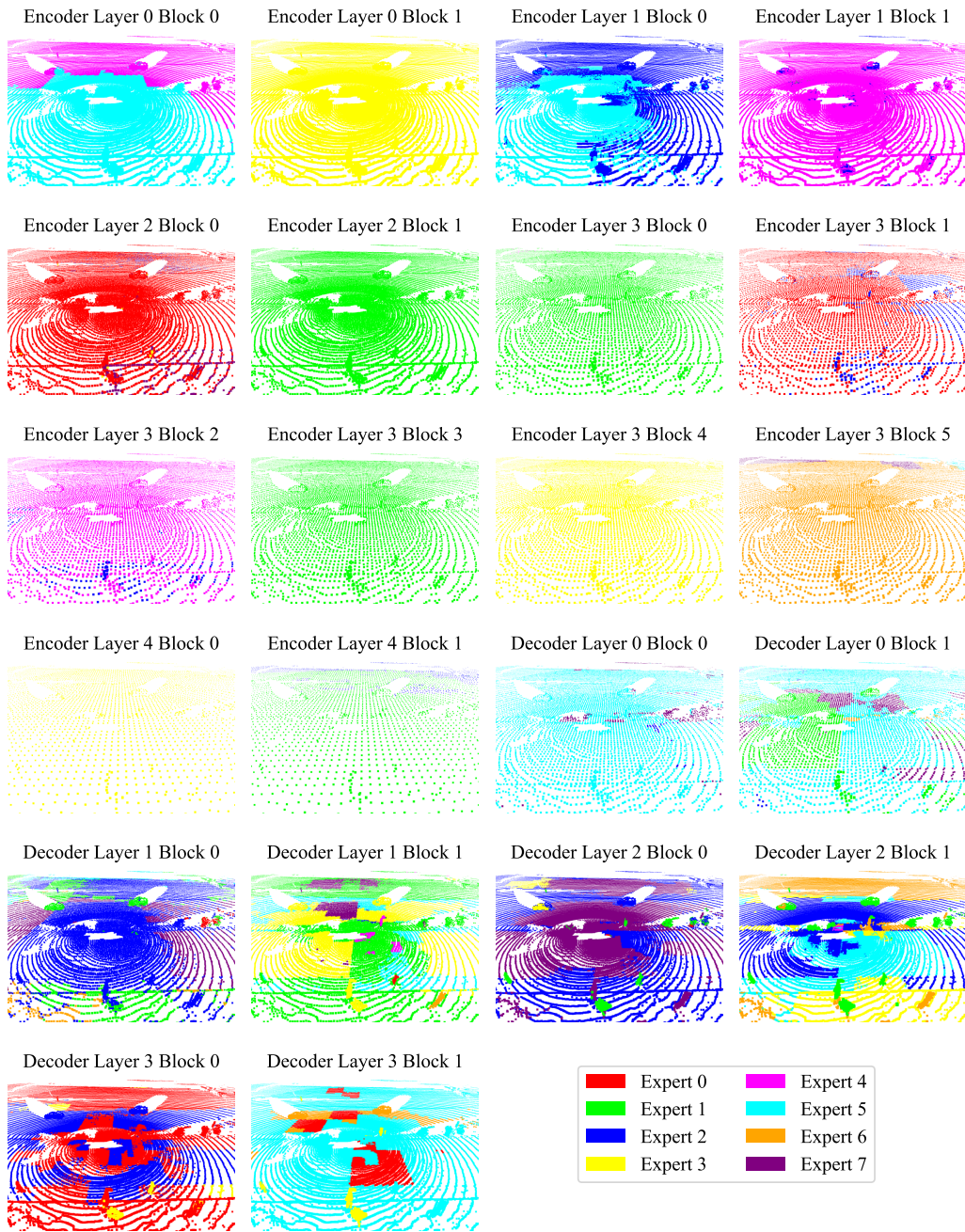


Figure 18: **Point-MoE’s Expert Choice Visualization on Waymo.** Color indicates the expert each point is assigned to across encoder and decoder stages. Early network layers maintain structured expert routes, but this structure relaxes in deeper layers, illustrating evolving internal representations.